



Temporal evolution of the efficiency of particle acceleration in supernova remnants

TO Machipi



orcid.org 0000-0002-5989-733X

Dissertation submitted in partial fulfilment of the requirements
for the degree *Master of Science in Astrophysical Sciences* at
the North-West University

Supervisor: Dr I Sushch

Co-supervisor: Dr P Goswami

Examination: November 2024

Student number: 38336308

Acknowledgements

Throughout the writing of this dissertation, I have received a lot of support and assistance. I would like to express my deepest gratitude to **Dr. Iurii Sushch** and **Dr. Pranjupriya Goswami**, my supervisor and co-supervisor, respectively. Their expertise and guidance were instrumental in shaping the research questions and methods of this study. Their insightful feedback consistently pushed me to refine my ideas and enhance the quality of my work, especially during moments when I struggled with this new research direction. I am deeply grateful for their patience and support.

I also would like to extend a special thanks to **Professor Elena Amato** from INAF - Osservatorio Astrofisico di Arcetri for the valuable discussions and engagements we had regarding my project during the HEASA conference. Her insights and suggestions were greatly appreciated.

I also would like to extend my heartfelt thanks to my dear friends, **Jane Letsoalo** and **Dakalo Phuravhathu**. Your unwavering support and encouragement guided me through the most challenging moments of this journey. You were my pillars of strength, offering motivation and believing in me when I needed it the most. Your constant presence, understanding, and wisdom words made the toughest days manageable. I could not have done this without your friendship and I am incredibly lucky to have you on my side.

Moreover, I express my sincere gratitude to the National Astrophysics and Space Science Programme (**NASSP**), the Centre for Space Research (**CSR**), and the **NWU** for their generous financial support.

Lastly, I dedicate this work to my mother **Astercia Mesola Ngobeni**. Your unconditional love, support, and encouragement have been my greatest source of strength. You have always believed in me, even during the times when I doubted myself. Your sacrifices and tireless efforts have made this achievement possible, and for that I am forever grateful. This dissertation is as much yours as mine. Thank you, Mom, for everything.

Abstract

A vital sign of ongoing particle acceleration can be found in the cut-off energy of a supernova remnant's (SNR) synchrotron radiation spectrum. To determine the cutoff energy and get insight into the nature of particle acceleration at the early stages of SNR evolution, we carefully studied 10 young SNRs, including all historical SNRs, which allows us to constrain the Bohm factor for each remnant. We are studying the temporal evolution of the acceleration efficiency and how some SNRs are limited by cooling and some by age. Our results reveal a clear distinction between SNRs limited by age and those limited by cooling. Younger remnants, such as **G1.9+0.3**, **RX J1713.7-3946**, and **G330.2+1.0**, exhibit high cut-off and maximum electron energies, suggesting efficient shock acceleration with minimal effects of synchrotron cooling. In contrast, older remnants like **Tycho**, **Kepler**, and **HESS J1731-347** show lower cutoff and synchrotron energies, indicating that synchrotron cooling significantly limits maximum particle energies. Furthermore, remnants such as **RX J1713.7-3946**, **RCW 86**, and **Vela Jr.**, with maximum synchrotron energies close to their observed cut-offs, are considered age-limited, although some cooling effects may still be present.

Our analysis of acceleration efficiency further suggests that the efficiency remains stable over time, contradicting models proposing linear evolution, with outliers such as **SN 1006** showing high efficiency and **HESS J1731-347** exhibiting low efficiency. These findings highlight the complexity of cosmic-ray acceleration and emphasize the need for more detailed modeling to understand the interplay of factors influencing particle acceleration and energy loss mechanisms in SNRs.

Keywords: Particle Acceleration; Cosmic Rays; Supernova Remnants; Galactic Astrophysical Sources.

Contents

1	Introduction	1
2	Supernova Remnants	4
2.1	Classification of Supernovae	4
2.1.1	Core collapse explosion	6
2.1.2	Thermonuclear explosion	8
2.2	Evolution of Supernova remnants	9
2.3	Observational evidence	11
3	Acceleration and Emission mechanisms	14
3.1	Diffusive shock acceleration	14
3.2	Synchrotron radiation	16
3.3	Inverse compton radiation	19
3.4	Pion-Decay radition	20
3.5	Turbulence in Supernova Remnants	20
3.5.1	The diffusion coefficient	21
	Bohm diffusion	21
3.6	ZA07 and SRCUT Models in X-ray Spectral Fitting	21
3.6.1	ZA07 Model: Electron Energy Distribution in Cooling-Limited Synchrotron Radiation	21
	Model Description	22

Key Features of the Model	22
Model Assumptions	22
Implications and Applications of the Model	23
3.6.2 SRCUT Model: Electron Energy Distribution in Age Limitation	23
Model Assumptions	24
4 X-ray data analysis	26
4.1 Observations and Data Reduction	26
4.2 Spectral Analysis	27
4.2.1 Synchrotron dominated spectra	35
5 Results	36
5.1 ZA07 Model	36
5.1.1 Acceleration efficiency for ZA07 model	36
5.1.2 Magnetic Estimates for ZA07 model	37
5.2 SRCUT Model	39
5.2.1 Acceleration efficiency for SRCUT model	39
5.2.2 Magnetic Estimates for SRCUT model	41
6 Discussion	44
6.1 Maximum Attainable Energy	44
6.1.1 Equating Synchrotron Cooling Timescale to the Age of a Supernova Remnant	45
6.2 Evolution of η	48
7 Conclusions and Outlooks	50
7.1 Conclusions	50
7.2 Outlooks	51

A DataSet	62
B Thermal Parameters	66

List of Figures

2.1	The categorization of supernovae, derived from optical spectroscopy and the shape of their light curves (Minkowski (1964))	5
2.2	Left: Supernovae generate the most abundant X-ray-emitting elements. The squares and the black line represent the average yield for core-collapse supernovae, while the circles show the yields for thermonuclear supernovae (red for the W7 deflagration model, and magenta for the WDD2 delayed detonation model). The model yields are taken from Iwamoto et al. (1999). Right: Oxygen yield from core-collapse supernovae relative to main sequence mass. Predictions from Woosley and Weaver (1995) are shown as circles and squares, from Chieffi and Limongi (2004) as triangles, and from Thielemann et al. (1996) as crosses. Typically, the oxygen yields from various models are quite similar, but above $30 M_{\odot}$, some models from Woosley and Weaver (1995), with 10^{51} erg explosion energies, predict a decrease in oxygen yield. This is because stellar cores above $30 M_{\odot}$ may collapse into black holes, and part of the oxygen is accreted by the black hole. The extent of fall-back is influenced by the explosion energy and the amount of mass loss before the supernova, as well as the numerical handling of the explosion.	6
2.3	The images illustrate, from top left to bottom right, the radio, X-ray (SNRcat 2020), low-energy gamma-ray (Federici et al. (2015)), and VHE gamma ray (Abdalla et al. (2018)) emission maps of the Galactic SNR G347.3-00.5 (RX J1713.7-3946). The subfigure in the top right corner provides an enlarged view of the bright compact central object.	12
4.1	Flux images in nonthermal-dominated energy bands taken with Chandra for G1.9+0.3, Kepler, Tycho, G330.2+1.0, and HESS J1731-347	28
4.2	Flux images in synchrotron dominated energy bands taken with Chandra for SN 1987A, RX J1713.7-3946, RCW 86, SN 1006, and Vela Jr	29

4.3	The spectra of the selected regions of each SNR with the best-fit <i>ZA07</i> model. The spectra from the Chandra and NuSTAR observations are displayed in black and red, respectively. The figure include spectra G1.9+0.3, G330.2+1.0, HESS J1731-347, Kepler, and RCW 86.	31
4.4	The spectra of the selected regions of each SNR with the best-fit <i>ZA07</i> model. The spectra from the Chandra and NuSTAR observations are displayed in black and red, respectively. The figure include spectra SN 1006, SN 1987A, Tycho, Vela Jr., and RX J1713.7-3946.	32
4.5	The spectra of the selected regions of each SNR with the best-fit <i>SRCUT</i> model. The spectra from the Chandra and NuSTAR observations are displayed in black and red, respectively. The figure include spectra of G1.9+0.3, G330.2+1.0, HESS J1731-347, Kepler, and RCW 86.	33
4.6	The spectra of the selected regions of each SNR with the best-fit <i>SRCUT</i> model. The spectra from the Chandra and NuSTAR observations are displayed in black and red, respectively. The figure include spectra of SN 1006, SN 1987A, Tycho, Vela Jr., and RX J1713.7-3946.	34
5.1	Acceleration efficiency against age of SNRs from the <i>ZA07</i> model	37
5.2	Acceleration efficiency against age of SNRs from the <i>SRCUT</i> model, when $B=10\mu G$	40
5.3	Acceleration efficiency against age of SNRs from the <i>SRCUT</i> model, when B is different and taken from different papers	41
6.1	Acceleration efficiency against age of SNRs	48

List of Tables

4.1	Properties of the SNRs	26
4.2	Parameters obtained from the ZA07 model (excluding magnetic field and acceleration efficiency)	30
4.3	Parameters of the SRCUT model from various studies (excluding magnetic field and acceleration efficiency).	30
5.1	Magnetic field strengths (B_{low}) and acceleration efficiencies (η) for different regions based on ZA07 model predictions.	38
5.2	Values of η for various sources when $B = 10\mu G$	40
5.3	Magnetic field strengths (B , μG) and acceleration efficiencies (η) for various regions based on SRCUT model parameters. Approximate values are indicated by \approx , and ranges represent observational bounds.	42
6.1	Synchrotron parameters for selected SNRs, including maximum synchrotron energy, X-ray cutoff energy, roll-off frequency, and maximum electron energy, with $E_{e,\max}$ converted to TeV.	47
A.1	Table Log for Chandra Observations	62
A.2	Table Log for NuSTAR Observations	65
B.1	Thermal Parameters of ZAO Model	66
B.2	Thermal Parameters of SRCUT Model	67

Table of abbreviations

A table containing a list of abbreviations that will be used throughout the text.

DSA	Diffusive Shock Acceleration
SNRs	Supernova remnants
LASER	Light Amplification by Stimulated Emission of Radiation
Cas A	Cassiopeia A
IC	Inverse Compton
CC	Core Collapse
SN	Supernova
VHE	Very High-Energy
PD	Pion Decay
PC	Parsecs

Chapter 1

Introduction

In this chapter, we will introduce supernovae and supernova remnants and describe how the emissions of these supernova remnants can be observed in the wavebands. Supernovae are crucial in contemporary astrophysics. They are vital for the chemical development of the Universe and serve as one of the primary energy sources for the interstellar medium (ISM). A portion of this energy exists as cosmic rays, with an energy density of $1 - 2 \text{ eV cm}^{-3}$ in our galaxy, representing roughly one-third of the total energy density within the ISM. Supernovae, especially Type Ia supernovae, are fundamental in contemporary cosmology because of their luminosity, which permits detection at high redshifts (up to $z \sim 1.7$, [Riess et al. \(2007\)](#)). Their observation has led to the revelation that the expansion of the Universe is accelerating rather than slowing down. ([Perlmutter et al. \(1998\)](#); [Garnavich et al. \(1998\)](#)).

Supernova remnants (SNRs) are recognized for their ability to accelerate particles to extremely high energies ([Ackermann et al. \(2013\)](#)). They are also generally believed to be sources of Galactic cosmic rays (CRs), with energies reaching up to a few PeV. The confirmed acceleration of electrons to high energies at SNR shocks is demonstrated by the detection of nonthermal X-ray emission, which is attributed to the synchrotron radiation from these accelerated electrons. The gamma-ray emission observed can be explained by both leptonic processes, such as inverse Compton scattering of relativistic electrons on ambient radiation fields, and hadronic processes, such as ion-ion interactions followed by pion decay. Evidence from various SNRs strongly suggests that both processes occur, leading to the effective acceleration of both electrons and protons. Although the general particle acceleration mechanism in SNRs is well understood and is governed by Diffusive Shock Acceleration (DSA) theory, numerous details remain ambiguous and require further study. One such detail is the confinement of particles to the shock region, which significantly influences the efficiency of particle acceleration and the maximum energies that particles can achieve. Of course, the physical conditions evolve over the lifetime of an SNR, and this evolution impacts the SNR's capacity to accelerate particles.

The radiation from SNRs can be detected across nearly the entire spectrum, ranging from radio waves to very high-energy (VHE) gamma rays. Typically, SNR emissions are classified into thermal emissions, originating from the hot plasma within the SNR, and nonthermal emissions,

originating from particles accelerated to relativistic speeds by the SNR. These thermal and nonthermal emissions generally overlap, at least up to X-ray energies, and depending on the specific object, distinguishing between them can be challenging.

Differentiating the X-ray emission from SNRs is more challenging, as numerous X-rays might result from line transitions of the thermal plasma. Moreover, relativistic particles emit synchrotron radiation within similar energy ranges. The complexity increases as the synchrotron spectrum of the non-thermal particles often exhibits a cutoff at X-ray energies. Consequently, only a small percentage of SNRs have verified nonthermal X-ray emission (refer to Section 2.3 and related references).

The parameter η can be indirectly inferred by measuring the shock velocity and cutoff energy in the synchrotron X-ray spectrum (e.g. [Reynolds \(1998\)](#); [Zirakashvili and Aharonian \(2007\)](#)). The TeV-emitting SNR RX J1713.7-3946 is acknowledged as an accelerator that works at the highest efficiency (that is, the acceleration operates near the Bohm limit with $\eta = 1$; [Tanaka et al. \(2008\)](#); [Tsuji et al. \(2019\)](#)). Since the launch of NuSTAR in 2012, we have acquired spatially resolved hard X-ray spectra, allowing for accurate measurements of the cutoff energy. Although young SNRs are traditionally considered to be effective accelerators, recent NuSTAR observations have shown that the acceleration efficiency η varies significantly depending on the acceleration region and/or the specific object. NuSTAR observations reported that η is ~ 1 in the forward shock and between 3 and 8 in the reverse shock or reflection shock in Cassiopeia A ([Sato et al. \(2018\)](#)). Furthermore, η was found to be ~ 20 in the youngest galactic SNR, G1.9+0.3 ([Aharonian et al. \(2017\)](#)). To achieve a comprehensive understanding of particle acceleration in young SNRs, the discrepancies between G1.9+0.3 (~ 190 years), Cassiopeia A (~ 330 years) and RX J1713.7-3946 (~ 1600 years) must be addressed.

In this project, we will focus on probing the temporal evolution of acceleration efficiency through the investigation of X-ray spectra from SNRs of different ages. The observed cut-off energy and the shape of the cut-off provide valuable information about the maximum energy of accelerated particles and about the process that is limiting acceleration. This, in turn, provides insight into how efficient the acceleration is. Considering SNRs of different ages would allow us to study how this efficiency changes with time. A similar study utilizing X-ray data was recently conducted by [Tsuji et al. \(2020\)](#). However, their study is incomplete because they assumed that the acceleration in the considered remnants is limited by synchrotron cooling. Although this might be true for some of the studied remnants, it is not true for the others, as is evident from their results. We plan to build up on this study and further develop the method, considering models with negligible synchrotron cooling.

We analyze and measure the cutoff energies in the synchrotron radiation spectra of 10 young supernova remnants (SNRs), including the following: G1.9+0.3, Cassiopeia A, Kepler's SNR (abbreviated as Kepler), Tycho's SNR (Tycho), G330.2+1.0, SN 1006, RX J1713.7-3946, RCW 86, Vela Jr., HESS J1731-347, and SN 1987A. Most of these are historic, which allows their ages to be well-determined. This study is structured as follows: Section 2 provides the background theory of SNRs, and Section 3 describes the theories of acceleration and emission mechanisms.

The observational data analyzed in this work, including data reduction, imaging, and spectral analyses, are detailed in Section 4. Section 5 covers the results of the correlation analysis and presents our findings. In Section 6, we discuss our results and in Section 7, we summarize our findings and give an outlook for future research.

Chapter 2

Supernova Remnants

The following chapter provides a brief overview of the classification, evolution, and observational evidence of supernova remnants (SNRs). These remnants, which form from the explosion of a star into a supernova (SN), are detectable across multiple wavelengths through various emission processes. Records of these explosions, which can manifest as daytime-visible guest stars if they occur close enough to Earth, date back to 1300BC ([Stephenson et al. \(1977\)](#)). These guest stars appeared abruptly and usually faded within weeks. There are two primary mechanisms that can cause such stellar explosions: thermonuclear explosions of white dwarfs ([Mazzali et al. \(2007\)](#)) and core-collapse (CC) events of massive stars ([Heger et al. \(2003\)](#)). Each type can be further divided into subcategories and has distinct observational features, yet both share the common trait of accelerating the progenitor star's material to velocities of several thousand kilometers per second. The interaction between this high-velocity ejected material - which generally carries a kinetic energy of approximately 10^{51} erg - and the surrounding medium results in a blast wave that heats the ambient material to X-ray-emitting temperatures. Over thousands to tens of thousands of years, the outer blast wave decelerates as it interacts with the ambient material and dissipates once its speed aligns with the ambient sound speed ([Harkness and Wheeler \(1990\)](#); [Borkowski et al. \(2013\)](#)).

2.1 Classification of Supernovae

Supernovae have traditionally been classified on the basis of their spectral characteristics, specifically the presence or absence of hydrogen. In addition, an observational classification system is employed (Figure 2.1), originating from [Minkowski \(1964\)](#), who noted that certain supernovae lack hydrogen absorption lines in their spectra (Type I), while others exhibit them (Type II).

Type II supernovae are always core-collapse supernovae, whereas Type I supernovae can be either core-collapse or thermonuclear in nature. Thermonuclear explosions correspond to the Type Ia spectroscopic class [Elias et al. \(1985\)](#), characterized by Si absorption lines in their spectra. Type Ib and Ic supernovae are now recognized as explosions of stars that have lost

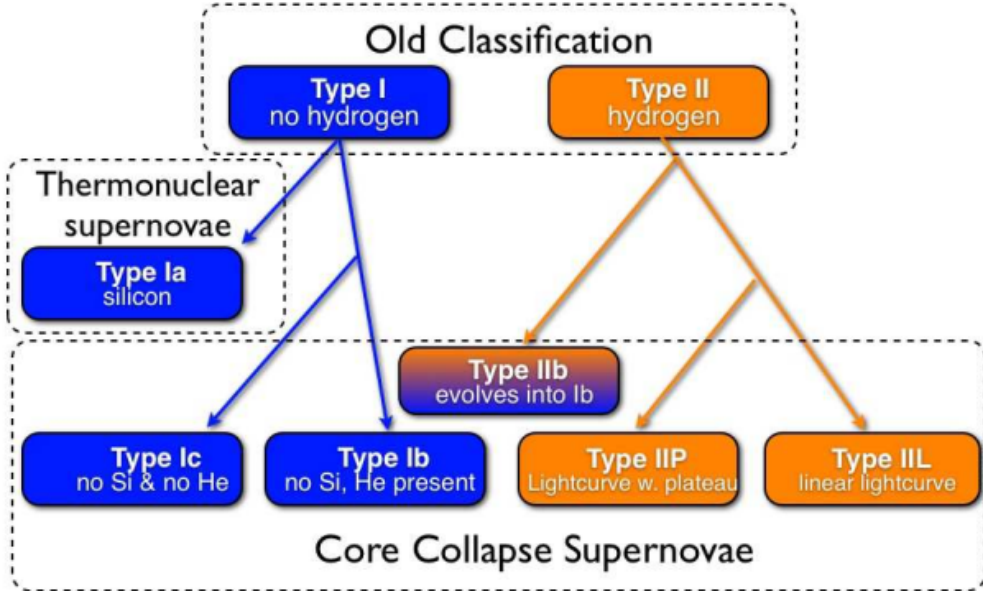


Figure 2.1: The categorization of supernovae, derived from optical spectroscopy and the shape of their light curves ([Minkowski \(1964\)](#)).

their hydrogen-rich envelope due to stellar wind mass loss [Heger et al. \(2003\)](#), or through interactions in binary star systems, e.g. [Podsiadlowski et al. \(1992\)](#). In the case of Type Ic, this mass loss appears to have also stripped away the helium-rich layers of the progenitor. The fact that these supernovae are predominantly located in the brightest regions of galaxies suggests that they are the explosions of the most massive stars, e.g. [Kelly et al. \(2008\)](#). In particular, long-duration gamma-ray bursts are also linked with Type Ic supernovae, e.g. [Galama et al. \(1998\)](#); [Stanek et al. \(2003\)](#).

The classification of Type II supernovae into Type IIP (plateau), Type IIL (linear light curve), and Type IIb is determined by two main observational criteria: optical spectroscopy and the light curve shape (Figure 2.1). Type IIP supernovae are the most frequently observed core-collapse supernovae, and optical observations of likely progenitor stars confirm that they originate from stars with initial masses in the $\sim 8 - 17 M_{\odot}$ range, exploding in the red supergiant phase while still retaining a significant hydrogen envelope (refer to discussions in [Smartt \(2009\)](#); [Chevalier \(2005\)](#)). Progenitors of Type IIL supernovae likely have a much less massive envelope due to mass loss from stellar winds or binary interactions. Type IIb supernovae are an intermediate type between Type Ib and Type II; initially, their spectra identify them as Type II, but over time, their spectra evolve to resemble those of Type Ib. This transition can be explained by extensive but incomplete loss of the hydrogen-rich envelope resulting from stellar winds or binary system interactions. The archetypal Type IIb supernova is SN 1993J ([Podsiadlowski et al. \(1993\)](#); [Woosley et al. \(1994\)](#)). In particular, the recent identification and subsequent spectroscopic study of the light echo from the supernova responsible for the well-studied supernova remnant Cassiopeia A (Cas A) indicates that it is a remnant of a Type IIb supernova, since its spectrum

exhibits both hydrogen and weak helium absorption lines ([Krause et al. \(2008\)](#)).

The Type IIn class is not included in Figure 2.1. Type IIn supernovae are identified by their narrow hydrogen emission lines, which are believed to originate from a dense circumstellar material, likely due to significant mass loss from the progenitor star. Its position in the diagram is somewhat uncertain because at least one Type IIn supernova, SN 2001ic, was initially classified as a Type Ia supernova but its spectrum later transformed into that of a Type IIn supernova ([Hamuy et al. \(2003\)](#)).

2.1.1 Core collapse explosion

Core collapse supernovae signify the terminal phase of massive stars, specifically those with main sequence masses $M \gtrsim 8M_{\odot}$ (see [Woosley and Janka \(2005\)](#) for an overview). Immediately preceding the collapse, the star exhibits stratified layers comprising the by-products of various sequential burning phases. Progressing from the core outward, one finds iron-group elements at the center (resulting from silicon burning), followed by silicon-group elements (products of oxygen burning), oxygen (a byproduct of neon burning), neon and magnesium (products of carbon burning), carbon (stemming from helium burning), helium (a product of hydrogen burning), and finally, outer layers of unprocessed hydrogen-rich compounds.

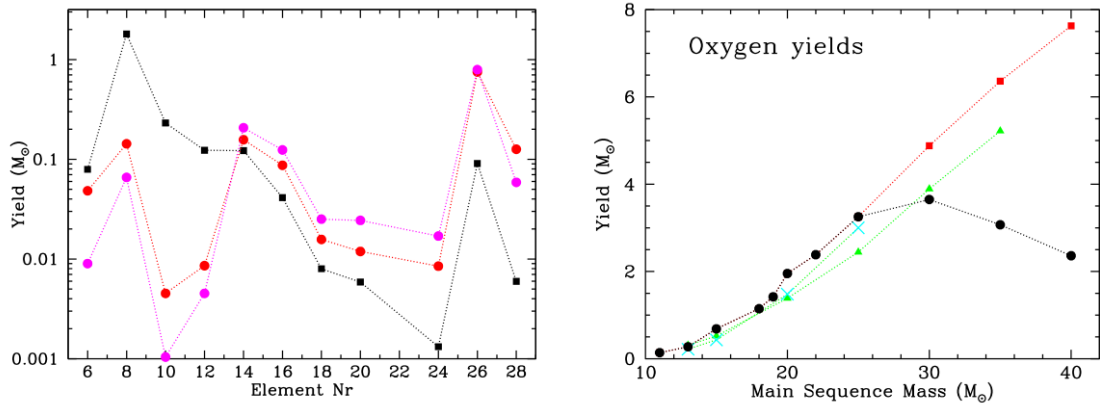


Figure 2.2: Left: Supernovae generate the most abundant X-ray-emitting elements. The squares and the black line represent the average yield for core-collapse supernovae, while the circles show the yields for thermonuclear supernovae (red for the W7 deflagration model, and magenta for the WDD2 delayed detonation model). The model yields are taken from [Iwamoto et al. \(1999\)](#). Right: Oxygen yield from core-collapse supernovae relative to main sequence mass. Predictions from [Woosley and Weaver \(1995\)](#) are shown as circles and squares, from [Chieffi and Limongi \(2004\)](#) as triangles, and from [Thielemann et al. \(1996\)](#) as crosses. Typically, the oxygen yields from various models are quite similar, but above $30 M_{\odot}$, some models from [Woosley and Weaver \(1995\)](#), with 10^{51} erg explosion energies, predict a decrease in oxygen yield. This is because stellar cores above $30 M_{\odot}$ may collapse into black holes, and part of the oxygen is accreted by the black hole. The extent of fall-back is influenced by the explosion energy and the amount of mass loss before the supernova, as well as the numerical handling of the explosion.

The formation of the iron-group core, which occurs over approximately one day, marks the star's

demise because iron fusion produces no energy. Consequently, the core collapses, becoming a proto-neutron star and, in the case of the most massive stars, a black hole. The majority of the released gravitational energy ($E \sim GM^2/R_{ns} \sim 10^{53}$ erg, with R_{ns} representing the neutron star radius) is emitted as neutrinos. This phenomenon was confirmed by neutrino detections from SN1987A using the Kamiokande (Hirata et al. (1987)) and Irvine-Michigan-Brookhaven (Bionta et al. (1987)) water Cherenkov detectors.

The exact mechanism for a supernova explosion, which demands the deposition of $\gtrsim 10^{51}$ erg of energy into the outer layers, remains unclear. The emergence of a proton star abruptly halts the collapse and generates a shock wave that propagates through the incoming material. However, according to numerical simulations, this shock wave falters. It is believed that the shock wave might be reinvigorated through the absorption of some of the neutrinos escaping the proto-neutron star, yet most numerical models that include neutrino absorption fail to replicate a supernova explosion (Janka et al. (2007)). Consequently, recent studies shift their attention toward the role of accretion instabilities in supernova explosions, as these instabilities could enhance neutrino absorption in specific regions just outside the proto-neutron star. One promising instability is the non-spherically symmetric standing accretion shock instability (SASI, Blondin et al. (2003)), which might also account for pulsar kicks and rotation (Blondin and Mezzacappa (2007)). Conversely, simulations by Burrows et al. (2007) propose that acoustic power, originating from g-mode oscillations within the proto-neutron star, leads to a successful explosion (but see Weinberg and Quataert (2008)). Additionally, there are theories that posit neutrino deposition is not the crucial factor for a successful explosion. Instead, the amplification of the stellar magnetic field, driven by differential rotation and compression, might result in the formation of magneto-centrifugal jets, which in turn ignite the explosion (Wheeler et al. (2002)).

The ejecta from core-collapse supernovae are mainly composed of stellar material, except for the innermost ejecta, which consist of products of explosive nucleosynthesis, predominantly Fe- and Si-group elements. These elements are formed from protons and alpha particles, which are the residuals of heavy elements that have broken down in intense heat around the collapsing core (Arnett (1996)). Some of these explosive nucleosynthesis products are radioactive, such as ^{56}Ni and ^{44}Ti and lines of these elements are used for the age estimation as they are unstable and decay quite fast. Notably, the energy produced by the decay of ^{56}Ni to ^{56}Co , and eventually to ^{56}Fe , heats the ejecta, significantly affecting the evolution of the supernova light curve. The yields of these elements are highly sensitive to the explosion's specifics, like the mass cut (the boundary between material that accretes onto the neutron star and material that is expelled), explosion energy, and asymmetry. Because the mass of the neutron star/black hole, the location of energy deposition and the presence of asymmetries are not well defined, the predicted yields of these elements are uncertain and vary greatly across different models (Fig.

refig:mesh2, Woosley and Weaver (1995); Thielemann et al. (1996); Chieffi and Limongi (2004)).

The primary products of core-collapse supernovae include carbon, oxygen, neon, and magnesium, which are formed during different phases of stellar burning (e.g., Woosley and Weaver

(1995); [Thielemann et al. \(1996\)](#); [Chieffi and Limongi \(2004\)](#)). The quantities of these elements depend on the initial mass of the progenitor star (Fig. 2.2).

2.1.2 Thermonuclear explosion

Type Ia supernovae are usually considered to be thermonuclear explosions of carbon-oxygen white dwarfs, meaning the energy of the explosion is derived from rapid nuclear burning, as opposed to gravitational energy released when a stellar core collapses.

While there is some fluctuation in the peak brightness of Type Ia supernovae, it is considerably less than that observed in Type II supernovae. This supports the notion that all Type Ia supernovae result from the explosive events of similar entities: C/O white dwarfs with masses near the Chandrasekhar limit ($1.38 M_{\odot}$). Furthermore, an observed relationship between their peak brightness and the post-peak decline rate of the light curve ([Phillips et al. \(1992\)](#)) allows for the calibration of their absolute peak brightness. Thus, Type Ia supernovae serve as excellent distance markers, providing substantial evidence for the accelerating expansion of the Universe ([Perlmutter et al. \(1998\)](#); [Garnavich et al. \(1998\)](#); [Riess et al. \(2007\)](#)).

There is no direct observational evidence linking white dwarfs to Type Ia progenitors. However, the occurrence of Type Ia supernovae exclusively in old stellar populations suggests that their progenitors are unlikely to be massive stars. The consistent nature of Type Ia supernovae can be most effectively explained by a progenitor with a narrow range of masses [Mazzali et al. \(2007\)](#). Additionally, C/O white dwarfs near the Chandrasekhar mass limit are strong candidates for Type Ia progenitors due to their high density, which provides the perfect conditions for a "nuclear fusion bomb" [Arnett \(1996\)](#). While the exact trigger mechanism remains unclear, the onset of a nuclear reaction in the core inevitably leads to an explosion.

A significant issue is our lack of knowledge regarding the most probable progenitor systems. It is evident that C/O white dwarfs need to accumulate matter to reach the Chandrasekhar threshold, meaning that thermonuclear supernovae must occur within a binary system. Nonetheless, this still allows for several possible progenitor systems: double degenerate systems (two white dwarfs) or white dwarfs paired with either a main sequence star or an evolved companion (i.e., single degenerate). Only a specific range of mass transfer rates, approximately $\sim 4 \times 10^{-8} - 7 \times 10^{-7} Myr^{-1}$, promote the stable growth of the white dwarf ([Nomoto \(1982\)](#); [Shen and Bildsten \(2007\)](#)). Novae, for instance, are relatively slow in accumulating mass and are thought to expel more mass than they collect. The only stable accretors among white dwarfs appear to be supersoft sources, but their population seems insufficient to explain the observed supernova rate (e.g., [Ruiter et al. \(2009\)](#)). Depending on the progenitor's development and accretion scenarios, the progenitor binary system may modify its surrounding circumstellar medium. For example, in the scenario of wind accretion, not all the mass lost by the donor will be captured by the white dwarf. [Hachisu et al. \(1999\)](#) suggested a scenario where Roche-lobe overflow from the donor star is stabilized via a rapid, optically thick wind from the white dwarf, which will also influence the immediate environment of the SNR.

Detonation-only models suggest that nearly all white dwarf material will be converted into iron-group elements. However, optical spectroscopy of Type Ia supernovae reveals that the ejecta include a substantial amount of intermediate-mass elements ([Branch et al. \(1982\)](#)). On the other hand, models of pure deflagration predict an excessive production of ^{54}Fe relative to ^{56}Fe and provide too narrow a velocity distribution for the intermediate-mass elements compared to what is observed. Consequently, the delayed detonation (DDT) model is currently the most favored model for Type Ia supernovae ([Khokhlov \(1991\)](#)). In this model, the explosion begins as a deflagration but transitions into a detonation wave, converting the remaining white dwarf into intermediate-mass elements (IMEs) such as silicon. Observations indicate that the fraction of burnt CO is approximately constant at $M = 1.1M_{\odot}$, but variations in peak brightness are due to the ratio of iron-group elements to IME products ([Mazzali et al. \(2007\)](#)) or the ratio of stable iron to ^{56}Ni ([Woosley et al. \(2007\)](#)). The decay of ^{56}Ni into ^{56}Fe generates heat that ultimately determines the brightness of a Type Ia supernova.

Figure 2.2 illustrates the expected overall abundance pattern for both the deflagration and DDT models. Unlike core-collapse supernovae, thermonuclear supernovae generate significantly larger amounts of iron group elements ($\sim 0.6M_{\odot}$). The explosion energy, E , of thermonuclear explosions is dependent on the mass of their burning products ([Woosley et al. \(2007\)](#)):

$$E_{51} = 1.56M_{Ni} + 1.74M_{Fe} + 1.24M_{IME} - 0.46 \quad (2.1)$$

where E_{51} represents the final kinetic energy measured in units of 10^{51} erg, and the masses of stable Fe, ^{56}Ni , and IME are expressed in solar masses.

2.2 Evolution of Supernova remnants

Despite the differences in the two described mechanisms of supernova explosions, both result in rapidly expanding stellar ejecta that interact with the surrounding material. The speed of the ejected material greatly exceeds the sound speed in the ambient medium. Consequently, the information about the approaching fast material cannot be transmitted to the material ahead - hereafter referred to as upstream - leading to the formation of a shock wave. This shock wave is distinguished by abrupt changes in density, pressure, temperature, and flow speed. The laws of conservation of momentum, mass, and energy across the shock surface result in conditions that connect the properties of the upstream and downstream medium, known as the Rankine-Hugoniot conditions ([Rankine \(1870\)](#)).

Immediately following a supernova (SN) explosion, a blast wave with an extremely high Mach number ($M \geq 10^3$) is generated, ejecting stellar material at velocities significantly exceeding the expected sound speeds in the adjacent interstellar medium (ISM) ([Reynolds \(2008\)](#)). The specific SN explosion discussed here is of type Ia (see [Reynolds \(2008\)](#) for detailed descriptions of different SN types), involving the nuclear burning of a carbon-oxygen white dwarf into iron-peak elements, releasing approximately $\sim 10^{51}$ erg of energy. This kinetic energy is deposited into the ISM surrounding the SN explosion. This forms a supernova remnant (SNR). The SNR's

evolution is typically simplified by categorizing it into four evolutionary stages ([Woltjer \(1972\)](#)).

1. *Free-Expansion Phase*: This phase is sometimes called the ejecta-dominated phase. During this time, the forward shock of the blast wave propagates into the ISM and accumulates mass as it moves outward. This phase continues as long as the mass of the ejecta remains significantly larger than the mass of the material being swept up ($M_{\text{ej}} > M_{\text{su}}$). For type Ia SNRs, the shock velocity in this phase is about $10^3 - 10^4 \text{ km s}^{-1}$ ([Reynolds \(2008\)](#)) and stays roughly constant until the swept-up mass equals the ejected mass. At this point, the accumulated mass starts to influence the SNR's expansion dynamics, signaling the end of the *Free-Expansion Phase*.
2. *Energy-Conservation Phase or Seydov-Taylor (ST) Phase*: The ST phase is also known as the adiabatic expansion phase. This phase starts when the swept mass, M_{su} , matches the ejecta mass, M_{ej} . The radius of the SNR at the beginning of the ST phase can be expressed as

$$R_{\text{ST}_0} = \left(\frac{3M_{\text{ej}}}{4\pi\mu\rho_0} \right)^{1/3} = 1.9 \left(\frac{M_{\text{ej}}}{n_0} \right) \text{ pc} \quad (2.2)$$

where $\rho_0 = n_0 m_H$ represents the mass density of the collected matter, n_0 denotes the pre-shock plasma density in the ISM into which the SNR is expanding, $\mu \approx 1.4$ is the average atomic weight of the ISM, and M_{ej} stands for the mass of the ejected material in solar masses (M_\odot). The ST phase is governed by the thermal pressure of the shock-heated gas that adiabatically expands into the ISM (preserving energy). The temperature of the shock-heated gas remains high enough that radiative losses are still quite ineffective. This phase is named in honor of [Sedov et al. \(1959\)](#), [Sedov \(2018\)](#)(which it is the updated publication), and [Taylor \(1950\)](#), who formulated a self-similar analytic model describing the shock's evolution during this phase for an explosion that injects energy instantaneously into a uniform density medium without energy dissipation. The self-similar ST solution is expressed as

$$R_{\text{ST}} = \zeta \times \left(\frac{E}{\rho_0} \right)^{1/5} t^{2/5} \quad \text{with } \zeta = 1.152 \quad (2.3)$$

Here, R_{ST} represents the radius of the SNR, E denotes the kinetic energy of the SN explosion, and t indicates the age of the SNR. Equation 2.3 is alternatively expressed as

$$R_{\text{ST}} \approx 0.314 \times \left(\frac{E_{51}}{n_0} \right)^{1/5} t_{\text{yr}}^{2/5} \text{ pc} \quad (2.4)$$

in which E_{51} denotes the kinetic energy produced by the SN explosion in units of 10^{51} erg, n_0 represents the pre-shock plasma density in the ISM in units of cm^{-3} , and t_{yr} represents the age of the SNR in years. This stage persists for approximately 10^4 years, with R_{ST} of the shock expanding to tens of pc. The ST stage concludes when the temperature has diminished sufficiently, through both expansion and adiabatic cooling, to allow recombination and enable the atoms to cool radiatively.

3. *Pressure-Driven Phase or Snow-Plough Phase*: During this phase, radiative losses become significant, rendering the conservation of energy assumption invalid. Instead, the shock wave's evolution is controlled by momentum conservation. Increased cooling slows the expansion of the SNR shell. In the region downstream of the shock, the hot gas has not yet cooled and continues to expand adiabatically, exerting pressure on the cooler outer shell. This pressure from the hot gas in the inner region applies force on the dense shell, effectively 'snow-ploughing' the ambient ISM mass outward, which maintains momentum conservation as the interior cools.
4. *Merging Phase*: When the velocity of the blast wave nears the sound speed or Alfvén velocity, the shock wave will gradually fade, allowing the shell to expand at subsonic speeds. This signifies the conclusion of the SNR, although remnants of its identity will persist for some time, as it has left behind a hot plasma bubble.

The basic model for the development of an SNR in the ISM is adequate to describe the broad observational characteristics of SNRs. Nevertheless, more sophisticated models are necessary to account for the specifics of individual SNRs. [Chevalier \(1974\)](#), [Truelove and McKee \(1999\)](#) are some of the authors who have elaborated on the dynamical progression of SNRs by incorporating factors such as the initial velocity or density profile of the ejecta, irregularities in the medium where the SNR is growing, energy loss due to the escape of CRs, and the influence of magnetic fields on expansion. Further details can be found in their works.

2.3 Observational evidence

Observational data has reinforced the role of supernova remnants (SNRs) as powerful sites of particle acceleration, making them key to understanding high-energy processes in the Galaxy. SNRs are not only remnants of explosive supernova events but are also thought to accelerate particles, potentially including cosmic rays (CRs), to extremely high energies. This connection between SNRs and CR acceleration aligns with both theoretical predictions and observed spectra, which often exhibit features characteristic of synchrotron radiation from accelerated particles. Since 1953, it has been recognized that SNR radio spectra include a non-thermal component, which can be interpreted as synchrotron radiation from relativistic electrons following a power-law distribution ([Shklovskii \(1953\)](#)).

Recent studies using advanced radio observations, particularly from the MeerKAT radio telescope, have identified around 200 new candidate supernova remnants (SNRs) in the Milky Way. This discovery significantly increases the number of known Galactic SNRs, which previously numbered approximately 300. If confirmed, these candidates would bring the total close to 500, helping address the discrepancy between the number of SNRs expected based on Galactic supernova rates and the number actually detected ([Michailidis et al. \(2024\)](#), [Merloni et al. \(2024\)](#), [Anderson et al. \(2024\)](#)). The radio emissions of these detected SNRs are invariably non-

thermal, serving as a criterion for classifying an object with extended radio emission as an SNR. In contrast, non-thermal X-ray emissions have been observed in only about a dozen remnants within our galaxy ([Cassam-Chenaï et al. \(2004\)](#); [Slane et al. \(1999\)](#); [Reynolds \(2008\)](#)).

The detection of nonthermal radio and X-ray emission suggests the existence of relativistic electrons within these remnants. To date, numerous remnants have been observed at gamma-ray energies by Fermi-LAT and imaging air Cherenkov telescopes (IACT) such as VERITAS, H.E.S.S., and MAGIC ([Acero et al. \(2015, 2016\)](#); [Abdalla et al. \(2018\)](#); [Archambault et al. \(2017\)](#); [Ahnen et al. \(2017\)](#)).

Figure 2.3 presents radio, X-ray and gamma-ray observation examples of one of the most luminous gamma-ray Galactic SNRs, RX J1713.7-3946. Generally, because of the excellent angular resolution of radio and X-ray instruments, SNRs appear as extended objects. Although RX J1713.7-3946 also appears extended in gamma-ray observations, this is not true for all Galactic SNRs, as some may be observed as point-like sources in gamma-ray instruments.

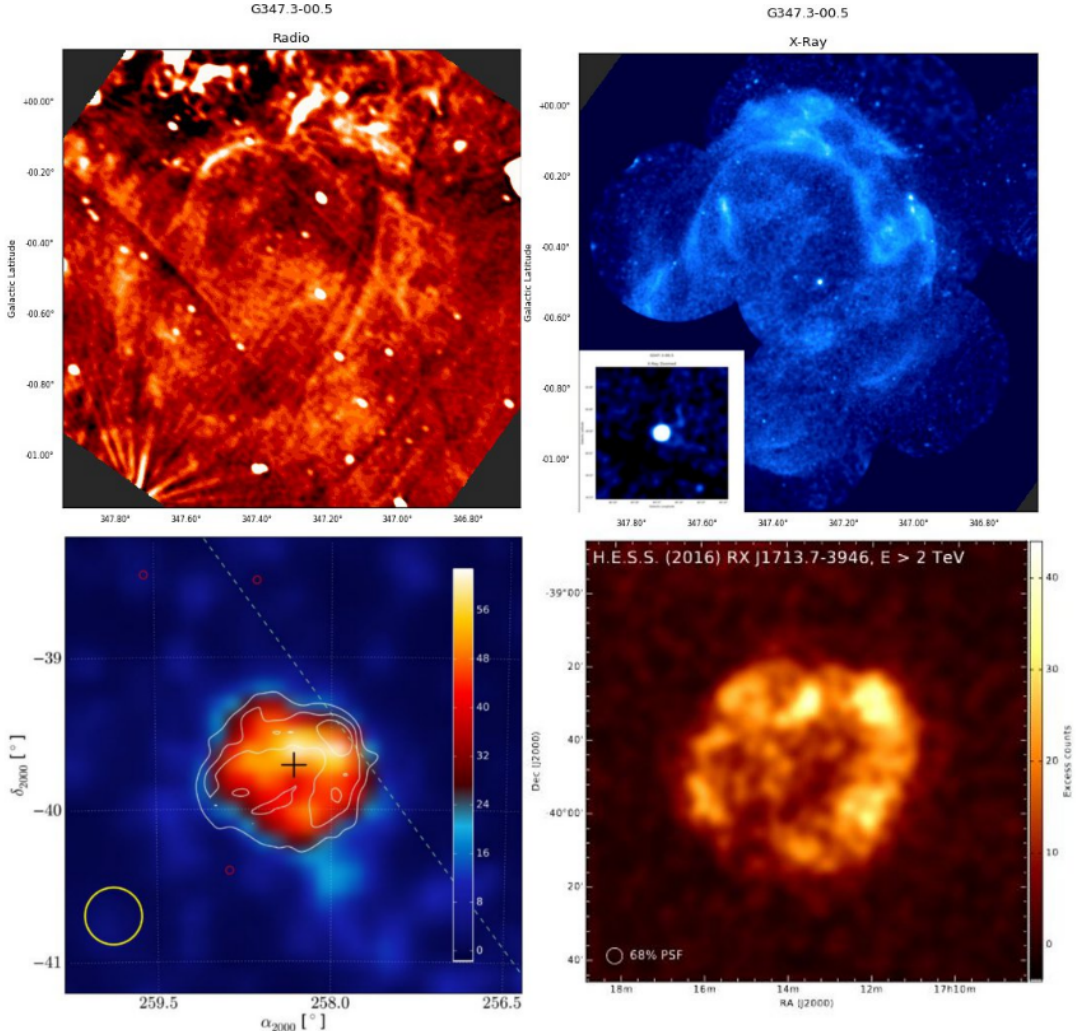


Figure 2.3: The images illustrate, from top left to bottom right, the radio, X-ray (SNRcat 2020), low-energy gamma-ray ([Federici et al. \(2015\)](#)), and VHE gamma ray ([Abdalla et al. \(2018\)](#)) emission maps of the Galactic SNR G347.3-00.5 (RX J1713.7-3946). The subfigure in the top right corner provides an enlarged view of the bright compact central object.

Gamma-ray emissions from SNRs may originate from either IC or pion decay. Differentiating between these processes in the gamma-ray spectrum is challenging, but Fermi-LAT ([Ackermann et al. \(2013\)](#)) detected a distinctive low-energy cutoff in the gamma-ray emissions from W44 and IC443 SNRs, suggesting a hadronic source. A leptonic source is unlikely as IC gamma-ray spectra are continuous power laws up to the VHE range. Here, either Klein-Nishina suppression or the cutoff of the electron spectrum could lead to the observed cutoff. Although the dependence of the spectral indices of the gamma-ray spectra on the underlying particle spectra varies between leptonic and hadronic processes, both scenarios are generally possible due to the unknown spectral indices of the particle spectra.

Studies of the magnetic field in SNRs utilize the width of synchrotron filaments ([Vink and Laming \(2003\)](#)) and indicate strong magnetic fields in SNRs, around hundreds of μG . The concept posits that these filaments result from the rapid energy loss of X-ray emitting electrons as they move away from the shock within the plasma flow. As their energy diminishes, they can no longer emit X-ray energies after covering a relatively short distance; thus, bright X-ray emissions are only seen in thin filaments near the shocks. Alternatively, these filaments can also be interpreted by considering lower magnetic fields if the field is attenuated downstream of the shock ([Pohl et al. \(2005\)](#)).

The radio spectra of SNRs provide further insights into the acceleration mechanisms. The majority of SNRs present a spectral index of $\alpha = 0.5$, implying a parent particle spectrum with a spectral index of $s = 2$. Nevertheless, α is centered around 0.5, with values primarily between 0.2 and 0.8. Younger SNRs tend to have spectral indices near 0.7, while older remnants exhibit indices closer to 0.5 or even higher ([Green \(2009\)](#); [Urošević \(2014\)](#)). The detected synchrotron spectra generally appear as simple power-laws or broken power-laws when significant synchrotron cooling modifies the parent electrons' spectral shape near the cutoff. There are, however, indications of slightly curved spectra in SNRs Tycho and Cas A ([Reynolds and Ellison \(1992\)](#)), suggesting additional effects that might influence the acceleration process.

Chapter 3

Acceleration and Emission mechanisms

In this chapter, we provide a concise overview of particle acceleration and radiation mechanisms relevant to supernova remnants. These include diffusive shock acceleration, synchrotron radiation, inverse Compton scattering, and pion-decay emission. Although all of these mechanisms are significant in the broader context, our study specifically focuses on synchrotron radiation. Additionally, we discuss turbulence in supernova remnants and outline the theoretical models employed in this study

3.1 Diffusive shock acceleration

The theory of diffusive shock acceleration (DSA) is widely regarded as an effective mechanism for accelerating cosmic rays in various astrophysical settings such as supernova remnants, active galactic nuclei, and gamma-ray bursts. The theory posits that particles can be trapped near the shock discontinuity through interactions with magnetohydrodynamic large-scale disturbances serving as scattering centers. The mean free path for scattering, λ_{sc} , is presumed to be significantly longer than the shock thickness and considerably shorter than the length L of the region with strong wave activity upstream and downstream. Consequently, particles are able to traverse the shock discontinuity repeatedly. Through these repeated interactions with converging scattering centers up- and downstream, charged particles gain energy. The shock compression ratio is defined as

$$r = \frac{\rho_2}{\rho_1} = \frac{U_1}{U_2} \quad (3.1)$$

where ρ_1 and U_1 represent the density and the fluid velocity before the shock upstream, while ρ_2 and U_2 symbolize the corresponding values after the shock downstream. The energy spectrum of particles that are accelerated by the shock eventually converges to the distribution described in Drury (1983)

$$f(p) \sim p^{-3U_1/(U_1 - U_2)} \sim p^{-3r/(r-1)} \quad (3.2)$$

with p representing the particles' momentum. In the case of strong shocks, the compression ratio is approximately $r \sim 4$, resulting in $3r/(r - 1) \sim 4$. This indicates that the exponent is solely dependent on the compression ratio and asymptotically approaches the value of 4, making DSA attractive for astrophysical plasmas.

The study of the energy gain δW for test particles crossing the shock discontinuity provides (refer to [Longair \(2011\)](#))

$$\frac{\langle \Delta W \rangle}{W} \sim \frac{Uu}{2c^2} \quad (3.3)$$

where U represents the shock velocity, u denotes the particle's velocity, and W is the particle's total energy. When the particle returns from the downstream region, it can cross the shock again, acquiring an additional energy increment of $(\frac{Uu}{2c^2})$. Thus, the average total energy gain for a particle completing one full cycle is

$$\frac{\Delta W}{W} \sim \frac{Uu}{c^2} \quad (3.4)$$

In the downstream vicinity, the scattering mechanism guarantees that the particle distribution remains isotropic. However, there are instances where the flow might carry particles away from the shock. Consequently, particles have a finite chance P_{esc} of escaping the downstream region. This escape probability can be determined as described in [Garrel et al. \(2018\)](#).

$$P_{esc} \approx \frac{U}{c} \quad (3.5)$$

Now, we define t_{up} , t_{dwn} , and t_{cycle} , which represent the average times a particle spends in the upstream region, downstream region, and the duration of a complete cycle across the shock, respectively ([Drury \(1983\)](#)).

$$t_{up} \sim \frac{\lambda_{sc_{up}}}{U} \quad (3.6)$$

$$t_{dwn} \sim \frac{\lambda_{sc_{dwn}}}{U/4} \quad (3.7)$$

$$t_{cycle} = t_{up} + t_{dwn} \sim \left(\frac{\lambda_{sc_{up}}}{U} + \frac{\lambda_{sc_{dwn}}}{U/4} \right) \sim \frac{\lambda_{sc_{up}}}{U} \quad (3.8)$$

(disregarding factors of 2). Given that the particles perform a random walk moving up and down their trail between the scatterers, the mean square displacement is expressed as

$$\langle R^2 \rangle = 6D_{up/dwn}t \quad (3.9)$$

where $D_{up/dwn}$ represents the diffusion coefficient in the upstream and downstream directions, respectively. By assuming that, we can approximate the relationship between the mean-free path and the diffusion coefficient for relativistic particles.

$$t = \lambda_{sc_{up/dwn}}/c \quad (3.10)$$

$$\begin{aligned} \lambda_{sc_{up}} &\sim \frac{D_{up}}{c} \\ \lambda_{sc_{dwn}} &\sim \frac{D_{dwn}}{c} \end{aligned} \quad (3.11)$$

It is apparent that t_{cycle} may also be expressed as

$$t_{cycle} \approx \frac{4}{c} \left(\frac{D_{up}}{U_1} + \frac{D_{dwn}}{U_2} \right) \sim \frac{D_{up}}{cU} \quad (3.12)$$

for particles moving at relativistic speeds ([Drury \(1983\)](#)), where U_1 and U_2 are specified in equation [3.1](#).

The rate of the energy gain of the particles is

$$\frac{\langle \Delta W \rangle}{dt} \sim \frac{U^2}{D_{up}} W \sim \frac{W}{t_{acc}} \quad (3.13)$$

Referring to equation [3.4](#) and substituting dt with t_{cycle} as indicated in equation [3.12](#), while assuming the particles travel at relativistic speeds, we can define the acceleration time as $t_{acc} \sim D_{up}/U^2$.

In conclusion, the energy distribution has been approximated as

$$N(E) \propto E^{-(1+t_{acc}/t_{esc})} \quad (3.14)$$

(as referenced in [Garrel et al. \(2018\)](#)), where the escape time t_{esc} is given by $t_{cycle}/P_{esc} \sim [D_{up}/cU]/[U/c] \sim D_{up}/U^2 \sim t_{acc}$ (as per equation [3.5](#), using t_{cycle} as the characteristic time scale) and t_{acc} is derived from equation [3.13](#).

3.2 Synchrotron radiation

Relativistic electrons spiralling within a magnetic field produce synchrotron radiation ([Lazarevich and Syrovatskii \(2013\)](#)). In numerous astrophysical scenarios, synchrotron radiation is generated by a nonthermal electron population, which is frequently well represented across a broad energy spectrum by a power-law distribution, notably when first-order Fermi acceleration is accountable for generating the relativistic electron populations.

Synchrotron radiation sources typically emit this radiation across a wide frequency range, spanning from low-frequency radio bands (~ 10 MHz) to X-rays ($\sim 10^{18}$ Hz). Most SNRs serve as radio synchrotron sources, with the radiation originating from the SNR shell. Composite SNRs also produce synchrotron radiation from embedded pulsar wind nebulae. Traditionally, X-ray synchrotron emission from SNRs was linked with pulsar wind nebulae; however, recent findings have shown X-ray synchrotron emission from young SNR shells ([Koyama et al. \(1995\)](#)).

An electron possessing relativistic energy E traveling through a magnetic field of strength B will produce synchrotron radiation, which peaks at a characteristic frequency ν_{ch} as demonstrated

by ([Ginzburg, Vitalii L and Syrovatskiĭ \(1966\)](#))

$$\begin{aligned}\nu_{ch} &= 1.8 \times 10^{18} B_{\perp} \left(\frac{E}{1 \text{ erg}} \right)^2 \\ h\nu_{ch} &= 13.9 \left(\frac{B_{\perp}}{100 \mu G} \right) \left(\frac{E}{1 \text{ erg}} \right)^2 \text{ keV}\end{aligned}\tag{3.15}$$

Consider $B_{\perp} \approx \sqrt{2/3}B$ as the component of the magnetic field perpendicular to the trajectory of the electron. In typical magnetic fields within Supernova Remnants (SNRs), where $B = 10 - 500 \mu G$, the electrons that emit have energies ranging from 10 to 100 TeV. These electrons might also be the source of several observed TeV gamma-ray emissions (e.g., [Aharonian et al. \(2001\)](#), [Aharonian et al. \(2004\)](#)). However, high-energy ions producing pions can also result in TeV gamma-ray emissions. There is ongoing discussion about which radiation mechanism is more prevalent in the TeV emissions from SNRs (refer to Hinton and Hofmann, 2009, for a detailed review).

The radiative losses for synchrotron radiation emitted by electrons occur at the following rate:

$$\begin{aligned}\frac{dE}{dt} &= -\frac{4}{3} \sigma_T c \left(\frac{E}{m_e c^2} \right)^2 \frac{B_{\perp}^2}{8\pi} \\ \frac{dE}{dt} &= -4.05 \times 10^{-7} \left(\frac{E}{100 \text{ TeV}} \right)^2 \left(\frac{B_{\perp}}{100 \mu G} \right)^2 \text{ erg s}^{-1}\end{aligned}\tag{3.16}$$

where σ_T represents the Thomson cross section. Typically, an additional term is added to B_{\perp} to account for losses due to inverse Compton scattering, replacing B_{\perp} with $B_{eff}^2 = B_{rad}^2 + B_{\perp}^2$. Here, $B_{rad} = 3.3 \mu G$, which is the value at which the magnetic field energy density is equal to the radiation energy density of the cosmic microwave background. This results in a synchrotron loss time scale of

$$\tau_{syn} = \frac{E}{dE/dt} = 12.5 \left(\frac{E}{100 \text{ TeV}} \right)^{-1} \left(\frac{B_{eff}}{100 \mu G} \right)^{-2} \text{ yr.}\tag{3.17}$$

For a group of relativistic electrons that exhibit a power law distribution of energy, the spectral index, α , of the synchrotron flux density spectrum correlates with the spectral index of the electron energy distribution, q , through $\alpha = (q - 1)/2$. Young supernova remnants (SNRs) typically have a radio spectral index around $\alpha \approx 0.5$, suggesting an electron energy distribution with $q \approx 2.2$, which aligns closely with predictions from the first-order Fermi acceleration theory. In the context of X-ray emission, the photon index Γ is more commonly used, defined as $\Gamma = \alpha + 1$. The X-ray synchrotron spectra of young SNRs usually exhibit rather steep indices, with Γ values ranging from 2 to 3.5. This steep gradient suggests that the synchrotron X-ray emission is primarily due to electrons near the maximum energy of the relativistic electron distribution. This maximum energy typically reflects scenarios where acceleration gains are balanced by radiative losses, often referred to as the loss-limited case. Alternatively, the electron

energy spectrum may truncate because the shock acceleration process has not persisted long enough for the electrons to achieve higher energies, known as the age-limited case (see [Reynolds \(1998\)](#)).

In the age-limited scenario, the electron spectrum shows an exponential energy cut-off $\propto \exp(-E/E_{max})$, while in the loss-limited scenario, the cut-off is predicted to be steeper $\propto \exp(-[E/E_{max}]^2)$ ([Zirakashvili and Aharonian \(2007\)](#)). Since the synchrotron emissivity function for a given electron energy has a notably broad spectral profile ([Ginzburg and Syrovatskii \(1965\)](#)), the steep cutoff in electron energies leads to a significantly more gradual rollover of the synchrotron spectrum.

$$n(h\nu) \approx (h\nu)^{-\Gamma} \exp\left(-\left[\frac{h\nu}{h\nu_{cut-off}}\right]^{1/2}\right) \quad (3.18)$$

By calculating the maximum electron energy in the loss-limited scenario, we obtain

$$\frac{E_{max}}{100TeV} \approx 0.32\eta^{-1/2} \left(\frac{B_{eff}}{100\mu G}\right)^{-1/2} \times \left(\frac{V_s}{5000km s^{-1}}\right) \left(\frac{\chi_4 - \frac{1}{4}}{\chi_4^2}\right)^{1/2}. \quad (3.19)$$

In the context of the equation provided, χ_4 is a dimensionless parameter that characterizes the efficiency and effectiveness of particle acceleration processes in astrophysical environments, such as shock waves in supernova remnants or active galactic nuclei. It may represent a compression ratio or a characteristic feature of the system, influencing how particles gain energy from magnetic fields and shock dynamics. The term $(\chi_4 - \frac{1}{4})^{1/2}$ suggests that this parameter must exceed a certain threshold ($\frac{1}{4}$) for the acceleration mechanism to be operational, indicating a non-linear dependence on the physical conditions governing the acceleration of the particles.

Substituting equation 3.19 into equation 3.18 demonstrates that the cut-off photon energy, $h\nu_{cut-off}$, does not depend on the magnetic field ([Aharonian and Atoyan \(1999\)](#)):

$$h\nu_{cut-off} = 1.4\eta^{-1} \left(\frac{\chi_4 - \frac{1}{4}}{\chi_4^2}\right) \left(\frac{V_s}{5000km s^{-1}}\right)^2 keV \quad (3.20)$$

Refer to [Zirakashvili and Aharonian \(2007\)](#) for a comprehensive derivation. This expression suggests that X-ray synchrotron radiation necessitates fairly high shock speeds ($\gtrsim 2000km s^{-1}$), which are typically found in young SNRs. Additionally, observing X-ray synchrotron radiation from SNR shells implies that the diffusion coefficients must not be significantly larger than those in the Bohm diffusion scenario.

3.3 Inverse compton radiation

IC radiation occurs when a high-energy electron impacts a low-energy photon, transferring energy to the photon and thus 'upscattering' it to higher energies ([Blumenthal and Gould \(1970\)](#); [Rybicki and Lightman \(1991\)](#)). Multiple interstellar radiation fields are present for upscattering by an electron population via the IC mechanism. These fields can include the CMB (with $T \approx 2.73$ K), FIR dust emission (with $T \approx 30$ K), and NIR stellar light (with $T \approx 300$ K). The CMB often represents the primary interstellar radiation field in the vicinity of an SNR; however, [Porter et al. \(2006\)](#) demonstrated that other interstellar radiation fields can significantly influence IC, particularly in the inner Galaxy or near star-forming regions. For a thermal photon field with a number density $n(\omega_i)$, where ω_i represents the incident photon energy,

$$n(\omega_i) = \frac{1}{\pi^2 \lambda^3} \frac{\omega_i^2}{e^{\omega_i/\Theta} - 1}, \quad (3.21)$$

where $\Theta = kT/m_e c^2$, and λ is called the Compton wavelength of the electron and is given by

$$\lambda = \frac{\hbar}{m_e c}. \quad (3.22)$$

Assuming $N_e(p)$ represents the momentum distribution of relativistic electrons within an isotropic photon field with number density $n(\omega_i)$, the differential photon-emissivity spectrum for a single photon can be expressed as

$$\frac{dn}{d\omega dt} = c \int n(\omega_i) d\omega_i \int_{p_{\min}}^{\infty} N_e(p) \sigma_{KN}(\gamma, \omega_i, \omega) dp, \quad (3.23)$$

where ω represents the energy of the upscattered photon, mathematically expressed as $\omega \equiv \frac{hu}{m_e c^2}$, and σ_{KN} denotes the Klein-Nishina scattering cross section as described by ([Jones \(1968\)](#); [Blumenthal and Gould \(1970\)](#); [Gould \(1975\)](#))

$$\sigma_{KN}(\gamma, \omega_i, \omega) = \frac{2\pi r_0^2}{\omega_i \gamma^2} \left[1 + q - 2q^2 + 2q \ln(q) + \frac{\Gamma^2 q^2 (1 - q)}{2(1 + \Gamma q)} \right], \quad (3.24)$$

and

$$q \equiv \frac{\omega}{4\omega_i \gamma (\gamma - \omega)} \quad (3.25)$$

for $\Gamma \equiv 4\omega_i \gamma$, and the classical electron radius, $r_0 = e^2/m_e c^2$.

3.4 Pion-Decay radition

PD radiation occurs when high-energy protons and ions, with approximately 280 MeV (Dermer et al. (2013)), interact with ISM material, resulting in the creation of charged and neutral pions (Pacholczyk (1970), Blumenthal and Gould (1970), Rybicki and Lightman (1991)). The neutral pions then promptly decay into two γ -ray photons,

$$p + p = \pi^0 + \gamma + \gamma, \quad (3.26)$$

with a rest energy of $\omega_0 = (m_\pi c^2/2) \approx 67.5$ MeV (Beringer et al. (2012)). Assuming $N_p(p)$ represents the differential proton distribution, the differential photon distribution can be expressed as

$$\frac{dn}{d\omega dt} = n_p \int v_p N_p(p) \frac{d\sigma(p_\pi, p)}{dp} dp, \quad (3.27)$$

where n_p represents the density of the target protons, $d\sigma(p_\pi, p)/dp$ denotes the cross section for the production of neutral pions in proton collisions, and v_p refers to the nonthermal proton velocity ((Dermer, 1986)). This distribution has a peak around 67.5 MeV, which corresponds to half of the rest mass of a neutral pion. Nevertheless, the peak is broadened because of Doppler shifting in the momentum distribution of the high-energy protons. This effect displays symmetry around the peak energy in a photon spectrum representation; however, when depicted in vF_v , it appears as a hardening of the spectrum at a few hundred MeV (Dermer et al. (2013), Stecker (1971)). This distinct π^0 -decay feature is termed the *pion-bump* and plays a crucial role in distinguishing γ -ray photons emitted by protons via PD from the commonly overlapping IC and bremsstrahlung spectra produced at γ -ray energies.

3.5 Turbulence in Supernova Remnants

Supernova remnants (SNRs) are some of the most energetic astrophysical regions, where strong shocks and magnetic fields interact to produce turbulence. This turbulence is essential in the acceleration and confinement of cosmic rays, affecting both the energy distribution and the spatial arrangement of these particles. In this section, we investigate the different forms of magnetic turbulence found in SNRs, their effects on particle acceleration, and the processes through which they confine particles near the shock front. The magnetic field within the SNR is significant for particle acceleration for two main reasons. Firstly, it determines the diffusion coefficient for the particles. Secondly, electrons lose energy by emitting synchrotron radiation, and the magnetic field dictates both the rate of energy loss and the emission spectra.

3.5.1 The diffusion coefficient

The diffusion coefficient is an essential factor in the acceleration process, determining both the acceleration time scale and the maximum energy that the particles can attain. Moreover, it influences the spatial distribution of cosmic rays, which could impact the emissions generated by the accelerated particles. Highly energetic electrons may escape regions with strong magnetic fields (for more details, visit [Sushch et al. \(2018\)](#)), leading to reduced synchrotron emission and decreased energy loss. Consequently, a discrepancy will arise between the synchrotron and IC emission maps.

Bohm diffusion

Bohm diffusion is recognized as the most effective diffusion regime because the diffusion length is equivalent to the gyro-radius of the particles. Under these conditions, the diffusion coefficient for relativistic particles is given by

$$D(p) = \eta \left(\frac{pc^2}{3qB} \right), \quad (3.28)$$

where p denotes the particle's momentum, c is the speed of light, q represents the particle's charge, B is the magnetic field, and η , often known as the gyrofactor, signifies the quotient of the background magnetic energy density and the energy density in magnetic fluctuations. In this context, the mean free path of the particle is proportional to its gyroradius. It is commonly assumed that the mean free path cannot fall below the gyroradius, thus $\eta \geq 1$. The equality in this case indicates a turbulence level where the wave amplitudes are similar to the strength of the static magnetic field, $\delta B \sim B$, known as the Bohm limit.

The energy dependence of the diffusion coefficient significantly influences the cutoff shape of the particle spectrum. Therefore, the synchrotron cutoff shape observed in X-ray remnants serves as a method to limit the energy dependence of the diffusion coefficient.

3.6 ZA07 and SRCUT Models in X-ray Spectral Fitting

3.6.1 ZA07 Model: Electron Energy Distribution in Cooling-Limited Synchrotron Radiation

The model proposed by [Zirakashvili and Aharonian \(2007\)](#), hereafter referred to as the ZA07 model, provides a framework for describing synchrotron radiation from relativistic, cooling-limited electrons in environments such as supernova remnants (SNRs) and other shock-driven astrophysical sources. This model combines particle acceleration processes with radiative cooling, offering a theoretical basis for understanding observed synchrotron spectra in cases where

electron energy losses are primarily due to synchrotron radiation.

Model Description

The ZA07 model provides an expression for the electron energy distribution in systems where particles are accelerated by strong shocks and subsequently cooled by synchrotron radiation as they interact with magnetic fields. The expression for the model of synchrotron radiation from cooling-limited electrons, is given by:

$$\frac{dN_X}{d\epsilon} \propto \left(\frac{\epsilon}{\epsilon_0}\right)^{-2} \left[1 + 0.38 \left(\frac{\epsilon}{\epsilon_0}\right)^{1/2}\right]^{11/4} \exp\left[-\left(\frac{\epsilon}{\epsilon_0}\right)^{1/2}\right] \quad (3.29)$$

where ϵ_0 represents the cutoff energy parameter, setting the scale of energies where cooling significantly impacts the electron population and ϵ is the photon energy.

Key Features of the Model

- **Power-Law Injection Spectrum:** At lower energies ($\epsilon \ll \epsilon_0$), the distribution follows a power-law dependence $\left(\frac{\epsilon}{\epsilon_0}\right)^{-2}$, which is characteristic of electrons accelerated by shocks. This term represents the initial energy distribution of particles injected into the system by the shock. The equation 3.29 describes the synchrotron spectrum at high energies. The photon spectral index of -2 corresponds to the cooled spectrum of electrons which would have an electron spectral index of -3.
- **Exponential Cutoff:** At higher energies ($\epsilon \gtrsim \epsilon_0$), the cooling of the synchrotron significantly affects the electron distribution, leading to an exponential suppression term $\exp\left[-\left(\frac{\epsilon}{\epsilon_0}\right)^{1/2}\right]$. This reflects the rapid energy loss of high-energy electrons, which limits their presence in the source.

Model Assumptions

The ZA07 model is based on several key assumptions:

- **Strong Shock Compression:** The model assumes that electrons are accelerated at a strong shock with a compression ratio $\sigma = 4$, which is typical for strong astrophysical shocks. This compression ratio enhances the magnetic field downstream, resulting in stronger synchrotron radiation and efficient cooling.
- **Magnetic Field Ratios:** The parameter k , defined as the ratio of the upstream magnetic

field to the downstream magnetic field, is given by:

$$k = \frac{B_{\text{up}}}{B_{\text{down}}}$$

In the context of the model, this parameter determines how the magnetic field is enhanced in the shock's downstream region. For example, with $k = \sqrt{\frac{1}{11}}$, the downstream magnetic field B_{down} is larger than the upstream field by a factor of $\sqrt{11}$, indicating a significant compression effect that influences the synchrotron cooling rates and the shape of the electron spectrum.

- **Cooling-Limited Electron Distribution:** The model is designed for scenarios where synchrotron cooling is the dominant energy-loss mechanism, imposing a limit on maximum electron energies and defining the shape of the high-energy tail of the electron distribution.
- **Isotropic Random Magnetic Fields:** The downstream magnetic field is assumed to be random and isotropic due to turbulent processes induced by shock compression. This isotropy leads to unpolarized synchrotron radiation, consistent with the lack of preferred magnetic field alignment in the downstream region.

Implications and Applications of the Model

The ZA07 model describes the energy distribution of relativistic electrons in environments where synchrotron cooling dominates, such as young supernova remnants. The shape of this distribution significantly impacts the observed synchrotron spectrum, especially in X-rays, where cooling effects shape the spectral cutoffs and slopes. By adjusting parameters like ϵ_0 and k , the model allows predictions of spectral features and cutoff frequencies that depend on both the particle acceleration processes and the magnetic field characteristics of the environment.

This model is essential for interpreting observed spectra and for inferring properties of magnetic fields and particle acceleration mechanisms in shock-driven sources. Observations of SNRs, pulsar wind nebulae, and galaxy clusters often exhibit synchrotron spectra that align with the predictions of cooling-limited models like ZA07, making it a valuable theoretical framework for connecting physical models with high-energy astrophysical observations.

3.6.2 SRCUT Model: Electron Energy Distribution in Age Limitation

I will also utilize the SRCUT model, which is a built-in model within `xspec` and is commonly used to describe synchrotron radiation from a population of relativistic electrons in supernova remnants (SNR). In the `srcut` model, the energy distribution of electrons is approximated as Reynolds (1998):

$$N(E) \propto E^{-2} e^{-E/E_{e,\max}} \quad (3.30)$$

where:

- $N(E)$ is the number density of electrons with energy E ,
- In `srcut` model, the spectral index is a fitting parameter. It doesn't assume anything for the index. But we just freeze it at 0.5 for your the spectral fitting which corresponds to the electron spectral index of 2
- $E_{e,\max}$ is the maximum energy of the electrons, limited by the age of the remnant.

Model Assumptions

The `srcut` model is based on several key assumptions:

- **Exponential Cutoff:** The inclusion of the term $e^{-E/E_{\max}}$ reflects the assumption that there is a maximum energy to which electrons can be accelerated, beyond which their density falls exponentially. This cutoff arises from the finite age of the SNR and the associated energy losses ([Webb et al. \(1984\)](#)).
- **Homogeneous Magnetic Field:** The model assumes a homogeneous magnetic field within the SNR, which is necessary for producing a well-defined synchrotron emission spectrum. Variations in the magnetic field strength would complicate the spectrum and deviate from the predictions of the `srcut` model.
- **Nonthermal Emission:** The model is designed to explain nonthermal emission, which means that it focuses on the synchrotron radiation produced by relativistic electrons rather than the thermal radiation from the remnant. This distinguishes the `srcut` model from models that treat thermal emissions, which dominate at lower energies.

The roll-off frequency can be calculated as:

$$\nu_{\text{roll}} = 1.6 \times 10^{16} \left(\frac{E_{\max}}{10 \text{ TeV}} \right)^2 \left(\frac{B}{10 \mu\text{G}} \right) \text{ Hz}, \quad (3.31)$$

where B is the magnetic field strength in microgauss.

The `srcut` model provides a coherent framework for analyzing electron synchrotron emissions in SNRs, particularly in scenarios where the electron spectrum is limited by the age of the remnant. By incorporating both a power-law distribution and an exponential cutoff, the model effectively captures the essential features of the synchrotron spectrum, allowing for meaningful comparisons with observational data.

In [Tsuiji et al. \(2020\)](#), the authors encountered a problem when examining how the acceleration efficiency changes over time. They relied solely on the ZA07 model, which led to estimates

of $\eta < 1$ for some supernova remnants (SNRs), and based on their definition of η , it can not be less than one. And from their results it suggests that their model to fit these SNRs is not suitable. To address this issue, we will analyze synchrotron radiation in SNRs employing both the ZA07 and SRCUT models, as they offer complementary perspectives on particle acceleration and emission mechanisms (for further details and results, see Chapter 5 and Section 6.2). By comparing the outputs of these models side by side, I aim to evaluate parameter consistency, measure the impact of synchrotron cooling, estimate magnetic field strengths, and enhance my understanding of the primary emission processes in SNRs. This combined approach will strengthen the reliability of my conclusions and broaden the understanding of the physics underlying these cosmic events.

Interstellar absorption inside these models is considered by the TBabs model within xspec. The Chandra spectra are analyzed within an energy range of 0.5-7 keV. For the NuSTAR spectra, SN 1006, RX J1713.7-3946, and Vela Jr. are examined over an energy range of 3-20 keV, while G1.9+0.3 and SN 1987A are evaluated within 3-40 keV. We conducted spectral fitting of the broadband X-ray observations (i.e., Chandra and NuSTAR combined fitting) when the NuSTAR data were available. Although merging the Chandra and NuSTAR spectra provides a more accurate determination of ϵ_0 , relying solely on Chandra data for fitting reduces susceptibility to systematic errors. We verified this by independently determining the parameter ϵ_0 using Chandra and NuSTAR spectra alone, yielding results that align with those from the combined fit. These fitting results are illustrated in Figure 4.3, 4.4, 4.5, 4.6 and are detailed in Table 4.2, 4.3. xspec version 12.13.1 was used for the spectral fitting process.

Chapter 4

X-ray data analysis

This chapter presents data analysis, including observations and data reduction processes. We also discuss the spectral analysis, focusing on the synchrotron-dominated spectra of 10 selected supernova remnants (SNRs).

4.1 Observations and Data Reduction

We conducted analysis of 10 young SNRs using X-ray observations. To uncover trends in acceleration efficiency among these young SNRs, it is crucial that they exhibit strong synchrotron emission and have well-defined physical parameters such as age, distance, and shock speed. The selection of the following 10 SNRs was based on the criteria mentioned above: G1.9+0.3, Cassiopeia A, Kepler, Tycho, G330.2+1.0, SN 1006, RXJ1713.7-3946, RCW 86, Vela Jr. and HESS J1731-347 within our galaxy, as well as SN 1987A in the Large Magellanic Cloud. The known parameters of the 10 SNRs are listed in Table 4.1.

Name	Age	Distance	Shock Speed	References
G1.9+0.3	190 ± 50	~ 8.5	3600-13000	Borkowski et al. (2017)
Tycho	440	2.3	3200-4000	Williams et al. (2013)
Kepler	415	4 ± 1	3400-5700	Katsuda et al. (2008)
G330.2+1.0	700 ± 300	~ 5	3700-9100	Park et al. (2006)
SN 1006	1010	1.9 ± 0.3	3000-7200	Winkler et al. (2014)
RX J1713.7-3946	1600 ± 10	1	800-4000	Acero et al. (2017)
RCW 86	1835	2.8	1800-3000	Yamaguchi et al. (2016)
Vela Jr.	3000-1000	0.5 – 0.9	~ 2000	Allen et al. (2014)
HESS J1731-347	2500-14000	3.6 ± 0.4	~ 2500	Abramowski et al. (2011)
SN 1987A	30	51.4	~ 6700	Frank et al. (2016)

Table 4.1: Properties of the SNRs

We used archival X-ray data obtained from Chandra and NuSTAR for our analysis. The details of the data set are summarized in Tables A.1 and A.2 in Appendix A.

The observational data were reduced using the standard data reduction software and procedure of Chandra and NuSTAR instruments. We download all available data for the SNRs from the Chandra Data Archive (CDA) and the data were processed with the Chandra Interactive Analysis of Observations (CIAO) software, version 4.16, and the Chandra Calibration Data Base (CALDB), version 4.11.2¹. The hard X-ray NuSTAR data were downloaded from HEASARC² and the data were processed with NuSTAR Data Analysis NuSTARDASSoftware³ version 2.1.1 and CALDB version 20220105 incorporated within HEAsoft version 6.30. The observation details of these two instruments are reported in Tables A.1 and A.2 (Appendix A).

Figures 4.1 and 4.2 show the region images of Chandra data made using DS9. The energy band is configured to 0.5 – 7 keV for synchrotron-dominated SNRs (namely, G1.9+0.3, G330.2+1.0, SN 1006 and HESS J1731-347) and RCW 86, while it is set to 4-6 keV for SNRs with thermal emissions (such as Kepler and Tycho). For creating chandra images of some sources such as G330.2+1.0, RX J1713.7-3946, RCW 86, SN 1006, and Vela Jr., we combined their observations to match those in Tsuji et al. (2020). In the case of HESS J1731-347, we utilized the "dmcopy" command and applied energy constraints of 0.5 – 7 keV to obtain the complete frame image.

To extract spectra, we employed "specextract" for Chandra data and "nuproducts" for NuSTAR data. Figures 4.1 and 4.2 show the source regions, while the background spectra were derived from adjacent areas of the source unless otherwise noted. We set the parameter "extended=yes" for all NuSTAR spectra, except for SN 1987A, which aligns with a point-like source. Spectra from various epochs and detector modules were merged using "addspec" for NuSTAR and Chandra we merged the events and created just one spectra from all the pointings. Despite most of the SNRs in this study exhibiting expansion, the larger extracted regions, compared to their proper motion shifts, allowed safe merging of spectra from different epochs. Importantly, summing the spectra from different epochs remained unaffected by temporal evolution and response file variations across the field of view. This was verified by fitting spectra from different epochs simultaneously, which yielded consistent results when fitting the combined spectrum.

4.2 Spectral Analysis

We use XSPEC software (version 12.13.0c) to perform the Chandra and NuSTAR spectral fit and combined Chandra-NuSTAR fit whenever possible. To account for cross-normalization uncertainties in the combined fit ,we use a constant factor and fixed it at 1 for Chandra and vary it for NuSTAR. In addition, we used the ISM absorption model TBabs available in XSPEC with the appropriate choice of the neutral hydrogen column density (NH) value. The values are reported in Tables 4.2 and 4.3. NH values were estimated with an online tool using the LAB

¹<https://cxc.cfa.harvard.edu/caldb/>

²<https://heasarc.gsfc.nasa.gov/>

³<https://heasarc.gsfc.nasa.gov/docs/nustar/>

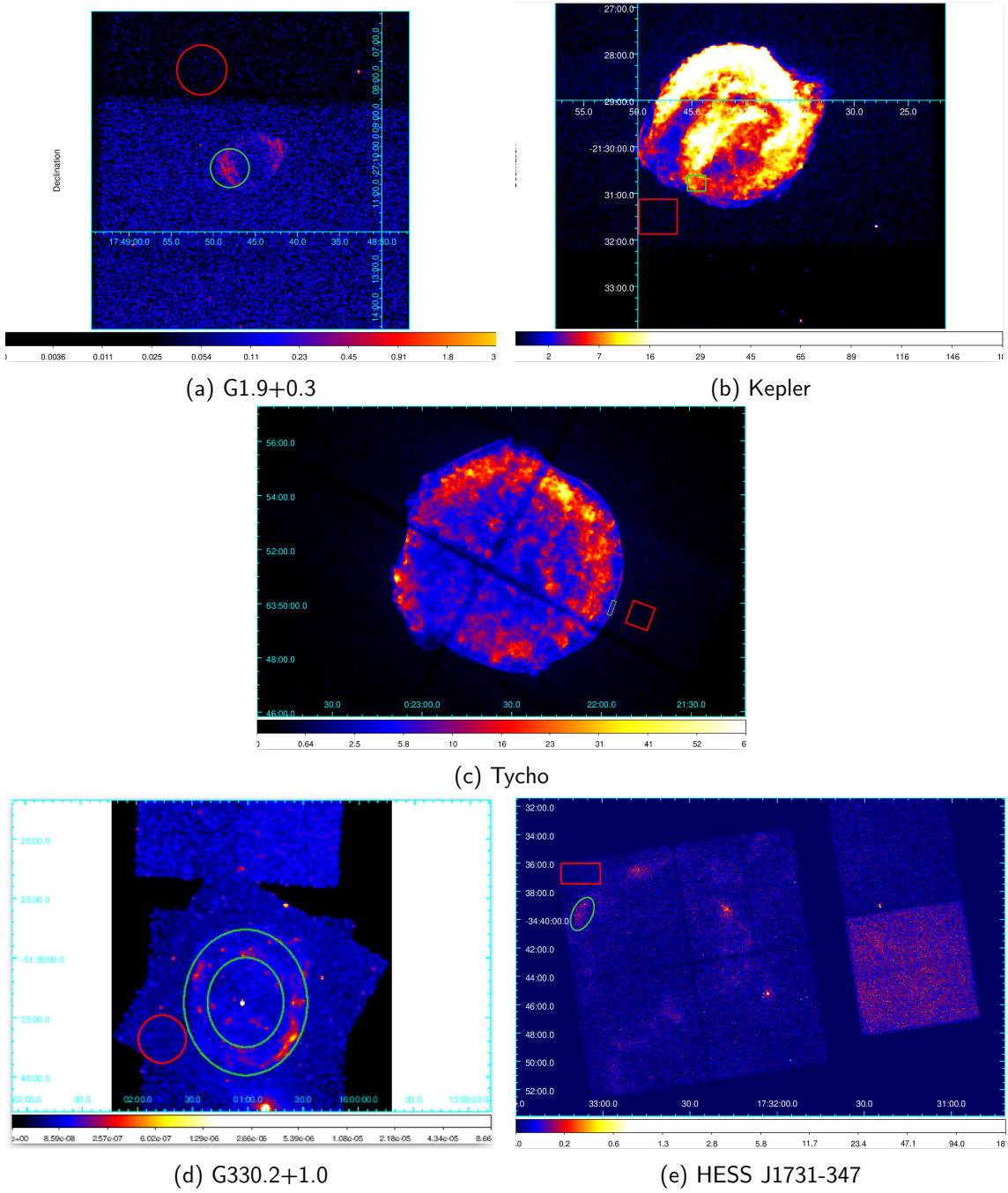


Figure 4.1: Flux images in nonthermal-dominated energy bands taken with Chandra for G1.9+0.3, Kepler, Tycho, G330.2+1.0, and HESS J1731-347

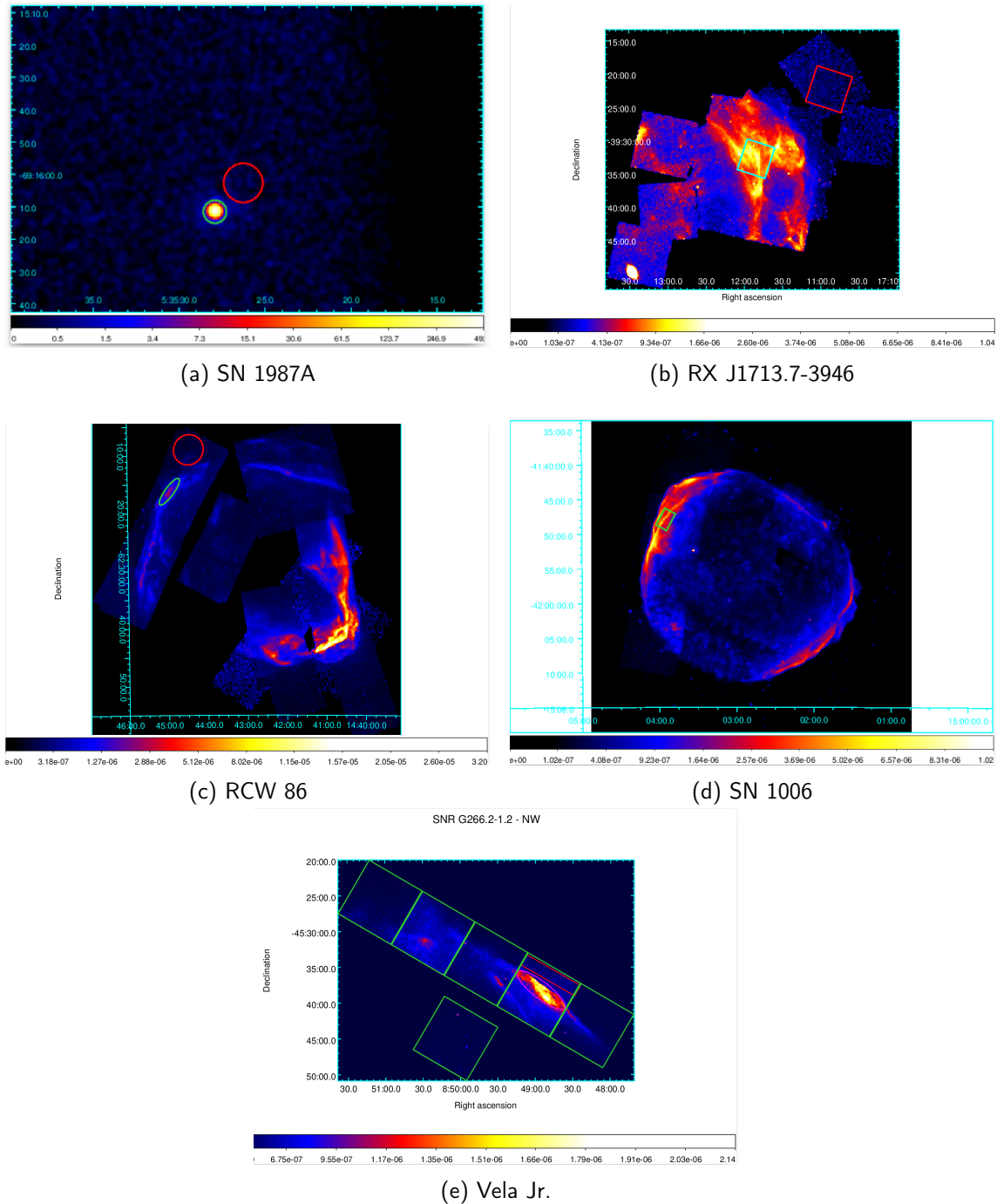


Figure 4.2: Flux images in synchrotron dominated energy bands taken with Chandra for SN 1987A, RX J1713.7-3946, RCW 86, SN 1006, and Vela Jr

survey map ([Kalberla et al. \(2005\)](#)).

We use two models, SRCUT (in-built in XSPEC) and ZA07 which is added to XSPEC as a local model using the numerical function given in Equation 3.29. The best-fit model parameters of the SRCUT and ZAO models are reported in Tables 4.2 and 4.3. Figures 4.3 and 4.4 illustrate the spectra obtained from the representative regions of each SNR using the ZA07 model, while Figures 4.5 and 4.6 illustrate the spectra obtained from the representative regions of each SNR using the SRCUT model. More details on models ZAO and SRCUT are discussed in Section 3.6.

NuSTAR spectra often exhibit uncertainties due to stray light. Consequently, we used NuSTAR data only for sources where this issue can be properly managed: specifically, for G1.9+0.3, SN 1006, RX J1713.7-3946, Vela Jr., and SN 1987A. The background spectrum observed with NuSTAR includes uncertainties from the non-uniform distribution caused by stray light and instrumental components ([Winkler et al. \(2014\)](#)), except in the case of RX J1713.7-3946, where the background was sufficiently subtracted as detailed in [Tsuji et al. \(2019\)](#). Since G1.9+0.3 and SN 1987A have small angular sizes, the background can be extracted from the surrounding area of the source, minimizing the impact of nonuniform background distribution on the results. For extensively extended sources such as SN 1006, RX J1713.7-3946, and Vela Jr., it is essential to carefully handle the non-uniform background. For more detailed studies on the background spectra in NuSTAR observations of SN 1006, Vela Jr., and RX J1713.7-3946, see [Li et al. \(2018\)](#), [Cesur et al. \(2018\)](#), and [Tsuji et al. \(2019\)](#), respectively.

Region	N_H (10^{20} cm $^{-2}$)	ε_0 (keV)	$\chi^2(dof)$	V_{sh} (km/s)
G1.9+0.3 (E)	5.897 ± 0.03	1.59 ± 0.1	853.61(582)	13000 ± 1000
SN 1987A (whole)	0.18 (fixed)	0.23 ± 0.01	368(315)	4800 ± 300
RX J1713.7-3946 (NW)	0.81 ± 0.02	1.58 ± 0.17	257(261)	3900 ± 300
HESS (NE)	1.0 (fixed)	0.886 ± 0.2	114(124)	2500 ± 1000
G330.2+1.0 (Whole)	2.5 (fixed)	1.564 ± 0.36	155.87(133)	7000 ± 2000
RCW 86 (NE)	0.33 (fixed)	0.275 ± 0.016	229.08(250)	2500 ± 700
Vela Jr (NW)	0.67 (fixed)	0.773 ± 0.1	390.18(286)	2000 ± 600
Tycho	0.574 ± 1.88	0.299 ± 1.128	248.63(268)	2500 ± 700
Kepler	0.36 ± 0.1	0.655 ± 0.24	111.76(123)	5727 ± 910
SN 1006 (NE)	0.116 ± 0.01	0.288 ± 0.03	516.97(439)	5500 ± 800

Table 4.2: Parameters obtained from the ZA07 model (excluding magnetic field and acceleration efficiency)

Region	N_H (10^{20} cm $^{-2}$)	V_{roll} (Hz)	$\chi^2(dof)$	V_{sh} (km/s)
G1.9+0.3 (E)	5.825 ± 0.04	$(3.83 \pm 0.20) \times 10^{17}$	852.35(582)	13000 ± 1000
SN 1987A (whole)	0.18 (fixed)	$(1.74 \pm 0.13) \times 10^{17}$	513(315)	4800 ± 300
RX J1713.7-3946 (NW)	0.78 ± 0.03	$(3.64 \pm 0.38) \times 10^{17}$	274(263)	3900 ± 300
HESS (NE)	1.0 (fixed)	$(1.93 \pm 0.38) \times 10^{17}$	114.4(124)	2500 ± 1000
G330.2+1.0 (Whole)	2.5 (fixed)	$(3.26 \pm 5.59) \times 10^{17}$	156.71(133)	7000 ± 2000
RCW 86 (NE)	0.33 (fixed)	$(0.57 \pm 0.05) \times 10^{17}$	225.76(250)	2500 ± 700
Vela Jr (NW)	0.67 (fixed)	$(1.54 \pm 0.13) \times 10^{17}$	373.86(286)	2000 ± 600
Tycho	0.616 ± 2.09	$(0.55 \pm 0.04) \times 10^{17}$	246.29(268)	2500 ± 700
Kepler	0.277 ± 0.117	$(1.80 \pm 0.85) \times 10^{17}$	111.98(122)	5727 ± 910
SN 1006 (NE)	0.115 ± 0.01	$(0.71 \pm 0.04) \times 10^{17}$	514.13(440)	5500 ± 800

Table 4.3: Parameters of the SRCUT model from various studies (excluding magnetic field and acceleration efficiency).

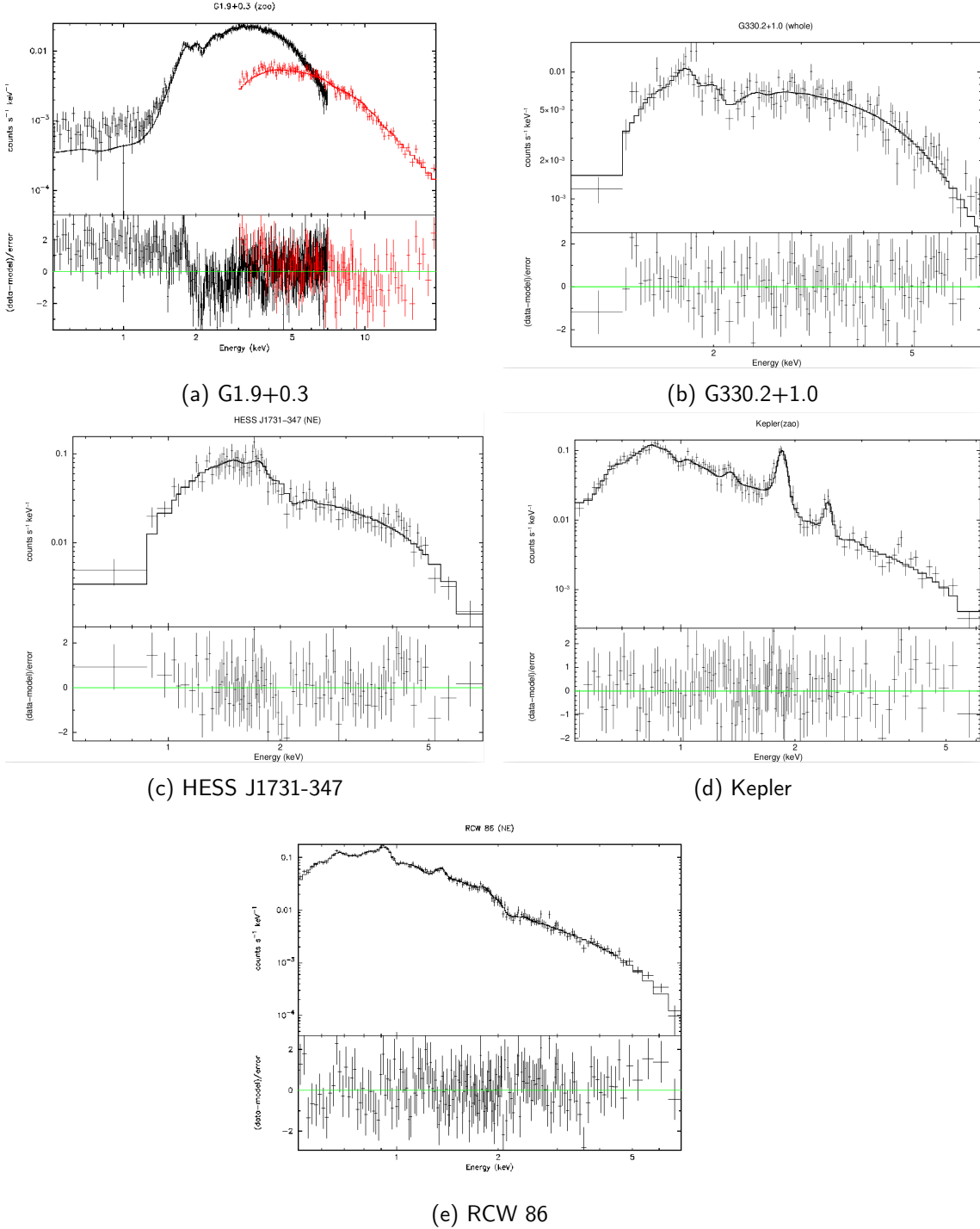


Figure 4.3: The spectra of the selected regions of each SNR with the best-fit ZA07 model. The spectra from the Chandra and NuSTAR observations are displayed in black and red, respectively. The figure include spectra G1.9+0.3, G330.2+1.0, HESS J1731-347, Kepler, and RCW 86.

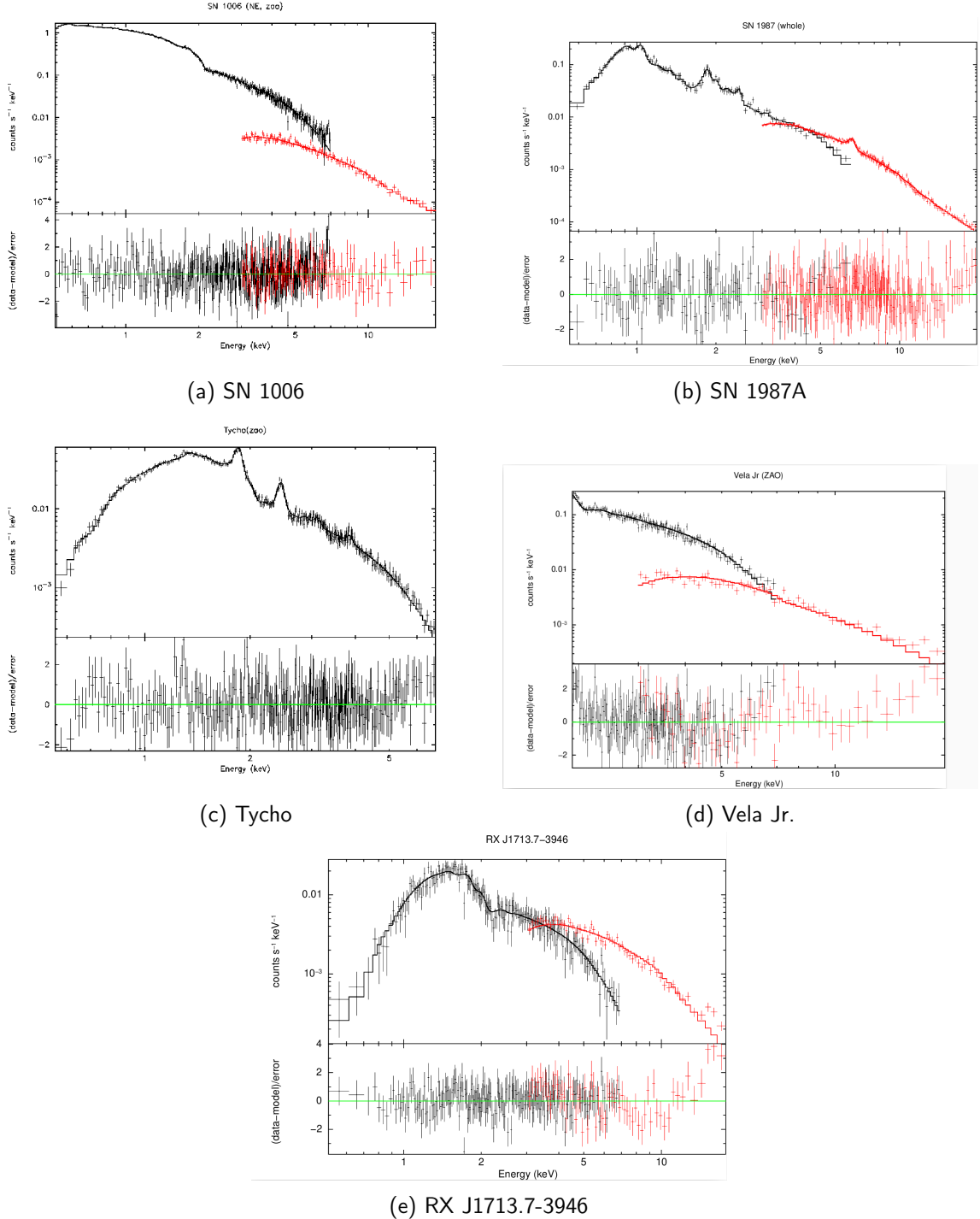


Figure 4.4: The spectra of the selected regions of each SNR with the best-fit ZA07 model. The spectra from the Chandra and NuSTAR observations are displayed in black and red, respectively. The figure include spectra SN 1006, SN 1987A, Tycho, Vela Jr., and RX J1713.7-3946.

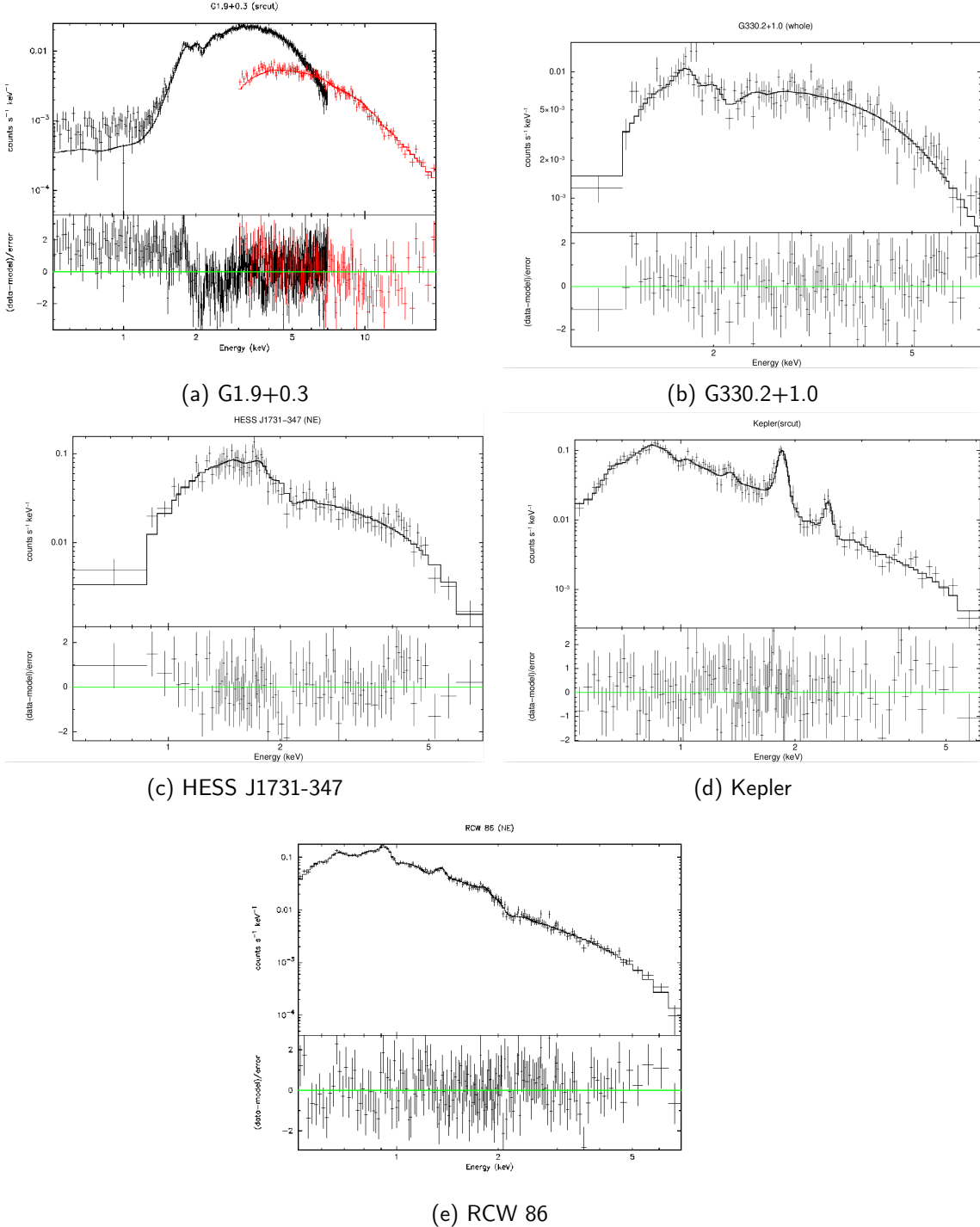


Figure 4.5: The spectra of the selected regions of each SNR with the best-fit *SR CUT* model. The spectra from the Chandra and NuSTAR observations are displayed in black and red, respectively. The figure include spectra of G1.9+0.3, G330.2+1.0, HESS J1731-347, Kepler, and RCW 86.

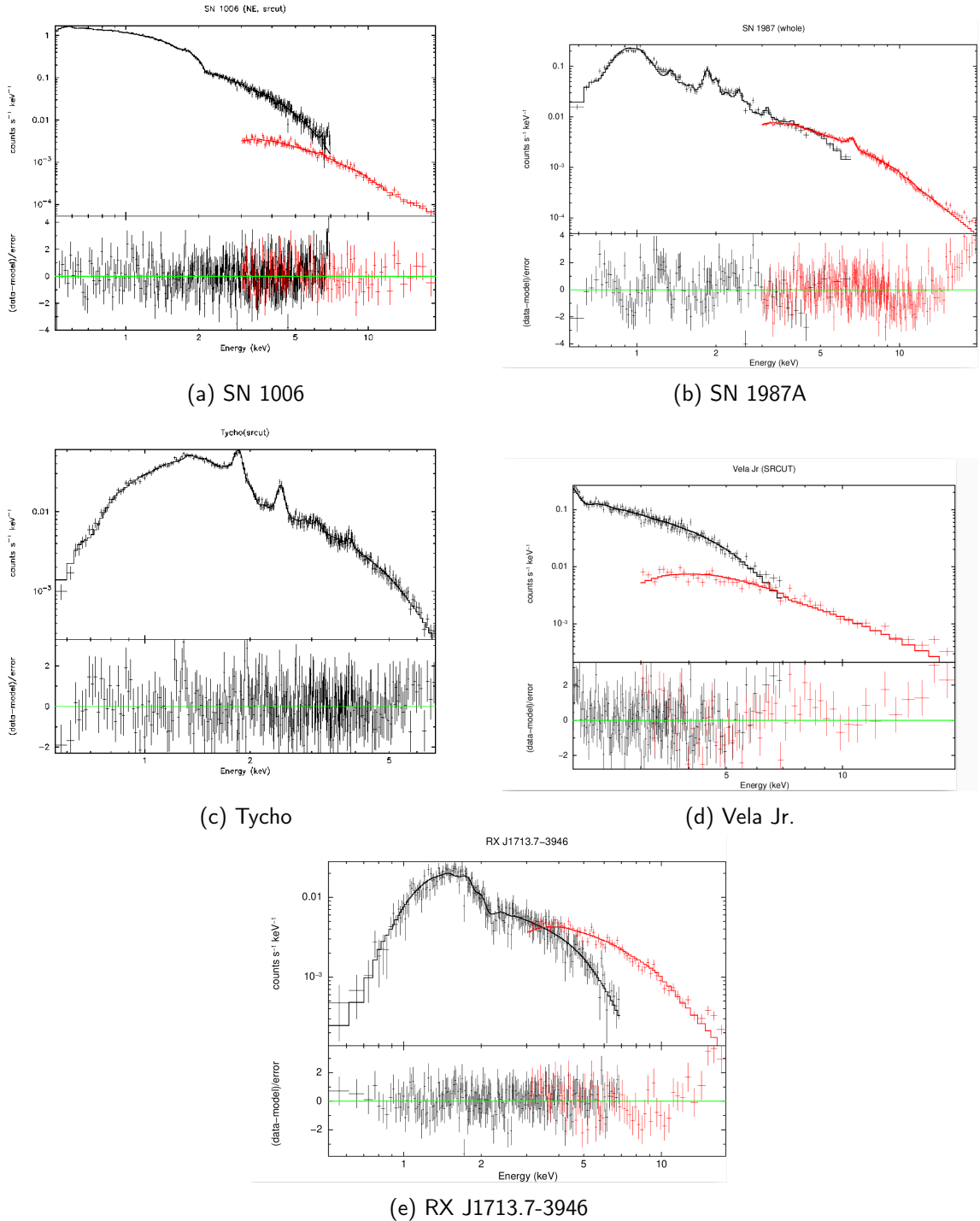


Figure 4.6: The spectra of the selected regions of each SNR with the best-fit *SRCUT* model. The spectra from the Chandra and NuSTAR observations are displayed in black and red, respectively. The figure include spectra of SN 1006, SN 1987A, Tycho, Vela Jr., and RX J1713.7-3946.

Certain SNRs exhibit strong thermal line emissions in addition to the synchrotron component, complicating the extraction of the pure synchrotron spectrum. For SNRs with thermal components, the 4-6 keV channel can be predominantly nonthermal radiation, whereas other X-ray bands could be tainted by thermal line emissions. The rims or filament-like structures, probably located in the outermost regions, shine brightly in the 4-6 keV energy band. These regions are believed to contain the synchrotron emission from electrons accelerated at the forward shock and are therefore optimal targets for our analysis of particle acceleration in SNRs. Regions were defined to extract spectra along these outer rims.

4.2.1 Synchrotron dominated spectra

X-ray spectra have the capability to provide limitations on particle acceleration mechanisms in SNRs, particularly where synchrotron emission is predominant. These types of entirely featureless nonthermal spectra have been observed in sources such as G1.9+0.3, G330.2+1.0, RX J1713.7-3946, Vela Jr., and HESS J1731-347. They are well reproduced by the absorbed ZA07/SRCUT model.

In certain spectra, significant thermal emission is observed in the cases of Kepler, Tycho, SN 1006, RCW 86, and SN 1987A. For these supernova remnants (SNRs), we incorporated a thermal model as an additive model in XSPEC, specified as TBabs \times (ZA07/SRCUT + thermal plasma). The thermal plasma is represented by VNEI for Kepler, and Tycho, while it is characterized by Vpshock in SN 1006 and RCW 86. In SN 1987A, we integrated a dual component thermal plasma model using Vpshock and Vequil (see, for example, [Frank et al. \(2016\)](#)). In the earlier three remnants, the plasma temperature (kT) and the ionization parameter (nt) are restricted to the values obtained from the reference areas shown in Figure 4.2. These thermal parameters are assigned based on the values found in the existing literature for SN 1006 ([Miceli et al. \(2009\)](#)), RCW 86 ([Tsubone et al. \(2017\)](#)), and SN 1987A ([Frank et al. \(2016\)](#)). The parameters pertaining to the thermal component are detailed in Tables B.1 and B.2 (Appendix B). Although the spectra are effectively modeled with this approach, it is possible that X-rays at higher energies are produced by thermal bremsstrahlung or a hot plasma rather than synchrotron radiation. It is important to mention that the origin of the hard X-ray component in SN 1987A remains unidentified.

In cases where supernova remnants (SNRs) displayed prominent thermal components, we performed additional fitting using solely the ZA07/SRCUT model, focusing on spectra exceeding 2.5 keV to minimize the influence of thermal components. We omitted the 6.4 to 6.8 keV channel if iron line emission was evident in the spectrum. The cut-off energy parameter remained relatively consistent across both approaches; however, the inclusion of the thermal model resulted in a marginally higher cutoff energy parameter.

Chapter 5

Results

In this chapter, we will give our results based on how the magnetic fields, the acceleration efficiency, and their constraints on the formulas were estimated. The Bohm factor, denoted as η , modifies the acceleration rate of the particles by accounting for deviations from the ideal Bohm limit. In the Bohm limit, particles experience maximum diffusion at the theoretically fastest rate, which is determined by the magnetic field strength. The Bohm factor η effectively scales the diffusion coefficient to reflect how close or far a system is from this limit, with $\eta = 1$ indicating Bohm diffusion and $\eta > 1$ representing slower sub-Bohm diffusion. To determine the low magnetic fields in subsection 5.1.2, we equate the cooling time (t_{syn}) with the age of a SNR (t_{age}), implying that the accelerated particles are initially injected and subsequently undergo cooling.

5.1 ZA07 Model

5.1.1 Acceleration efficiency for ZA07 model

In the present framework, the cutoff energy parameter ε_0 is crucial to characterizing shock acceleration in supernova remnants (SNRs), as it results from the balance between particle acceleration and synchrotron cooling losses. [Zirakashvili and Aharonian \(2007\)](#) derived a relation between the cutoff energy parameter and the shock velocity v_{sh} , showing that ε_0 is proportional to the square of the shock velocity and inversely proportional to the Bohm factor η , which describes the diffusion efficiency of the particles relative to the ideal Bohm limit. The equation

$$\varepsilon_0 = 1.6 \left(\frac{v_{sh}}{4000 \text{ km/s}} \right)^2 \eta^{-1} \text{ keV} \quad (5.1)$$

relates these quantities, allowing for the estimation of η when both ε_0 and v_{sh} are known. The Bohm factor

$$\eta = 1.6 \left(\frac{v_{\text{sh}}}{4000 \text{ km/s}} \right)^2 \left(\frac{\epsilon_0}{\text{keV}} \right)^{-1} \quad (5.2)$$

serves as an essential diagnostic tool for analyzing the proportion of total energy density within the magnetic field compared to that in the turbulent particle field, where the values of η provide insight into more effective diffusion. By integrating the calculated cut-off energy parameters with the shock velocities, one can estimate the Bohm factor η in various SNR regions, offering information on the differences in particle acceleration among these remnants.

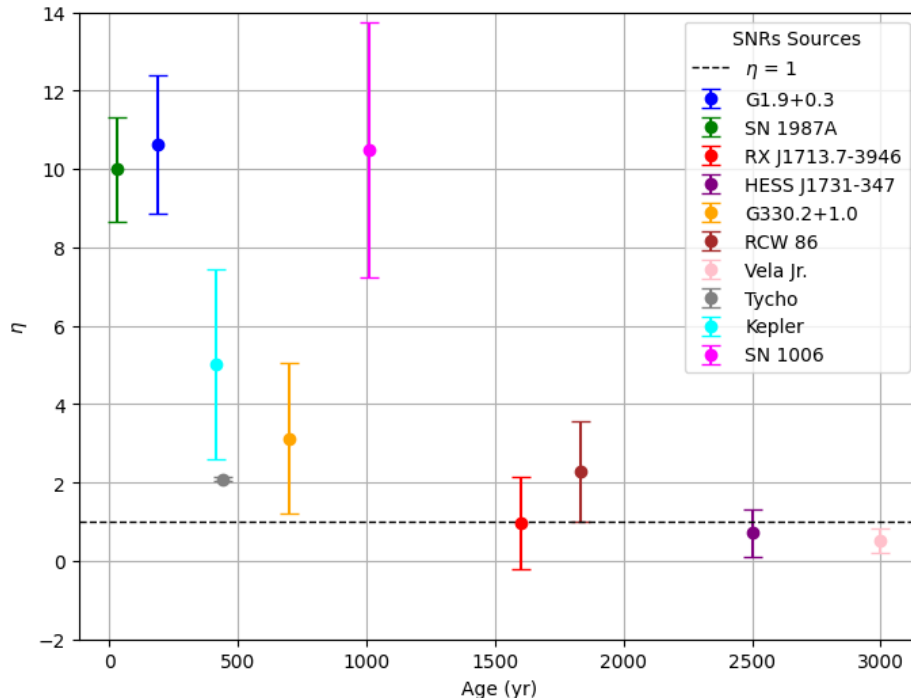


Figure 5.1: Acceleration efficiency against age of SNRs from the ZA07 model

In Figure 5.1 we show the relation of acceleration efficiency with age, and we observe that 7 SNRs (G1.9+0.3, SN 1987A, G330.2+1.0, RCW 86, Tycho, Kepler, and SN 1006) show a $\eta > 1$, while 3 SNRs (RX J1713.7-3946, HESS J1731-347, and Vela Jr.) show a $\eta < 1$. See their values in Table 5.1. It is important to note that, technically speaking, discussing Vela Jr contradicts the condition $\eta > 1$. The other two sources, RX J1713.7-3946 and HESS J1731-347, are in agreement with 1, considering the margin of error.

5.1.2 Magnetic Estimates for ZA07 model

In the synchrotron cooling-limited scenario (Zirakashvili and Aharonian (2007)), where the acceleration time scale τ_{acc} is approximately equal to the synchrotron cooling timescale τ_{synch} and is shorter than the dynamical timescale t_{age} , the condition for synchrotron emitting electrons can be expressed as:

$$\tau_{\text{acc}} \approx \tau_{\text{synch}} \leq t_{\text{age}} \quad (5.3)$$

Region	Magnetic Field (B_{low} , μG)	Acceleration Efficiency (η)
G1.9+0.3 (E)	54 ± 8	10.63 ± 1.77
SN 1987A (whole)	124 ± 15	10.0 ± 1.33
RX J1713.7-3946 (NW)	8.6 ± 0.6	0.96 ± 1.18
HESS J1731-347 (NE)	7.5 ± 4	0.71 ± 0.59
G330.2+1.0 (Whole)	18.5 ± 6	3.13 ± 1.93
RCW 86 (NE)	16.5 ± 2	2.27 ± 1.28
Vela Jr (NW)	6.6 ± 5	0.52 ± 0.32
Tycho	41 ± 13	2.09 ± 0.04
Kepler	38.0 ± 7	5.01 ± 2.43
SN 1006 (NE)	31.2 ± 5	10.50 ± 3.25

Table 5.1: Magnetic field strengths (B_{low}) and acceleration efficiencies (η) for different regions based on ZA07 model predictions.

This condition ensures that synchrotron cooling remains effective within the source's lifetime. By ensuring that $\tau_{\text{synch}} \leq t_{\text{age}}$, we can place a lower limit on the magnetic field B , which can be expressed as:

$$B \geq B_{\text{low}} = 12 \left(\frac{t_{\text{age}}}{1 \text{ kyr}} \right)^{-2/3} \left(\frac{u_1}{4000 \text{ km s}^{-1}} \right)^{-2/3} \eta^{1/3} \mu\text{G} \quad (5.4)$$

where:

- t_{age} is the age of the SNR in kiloyears (kyr),
- u_1 is the shock velocity in km s^{-1} ,
- η represents the acceleration efficiency.

This condition provides a lower bound on the magnetic field strength, ensuring that the synchrotron cooling-limited condition is satisfied. The smallest value of B for each region is listed in Table 5.1.

The magnetic fields observed in these SNR regions show a notable range, with higher fields generally associated with younger and more compact remnants, aligning with the trends observed in the study of [Tsuiji et al. \(2020\)](#). For instance, SN 1987A, with a strong magnetic field of $124 \pm 15 \mu\text{G}$, and G1.9+0.3 (E) with $54 \pm 8 \mu\text{G}$, exemplify the elevated magnetic field strengths often found in very young remnants. The effect of shock compression in very young remnants and those a few thousand years old tends to remain similar. Other factors, such as the expansion into the progenitor star's wind for core-collapse supernova remnants, might contribute to an enhanced magnetic field in very young SNRs. In theory, turbulence generation is expected to be more effective at the onset, resulting in a stronger magnetic field, although clear evidence supporting this is lacking.

In contrast, older or more evolved remnants such as Vela Jr (NW) and HESS J1731-347 (NE) exhibit much lower magnetic fields, at $6.6 \pm 5 \mu\text{G}$ and $7.5 \pm 4 \mu\text{G}$, respectively.

Midrange magnetic fields, as observed in remnants like Tycho and Kepler, around $38 - 41 \mu\text{G}$, align well with Tsuji's findings for SNRs that, while still young, they are not as compact or as energetically intense as the very youngest remnants, such as SN 1987A.

This variation in magnetic field strength across different SNRs underscores the impact of age and shock is getting slower, but it remains strong, meaning that the Mach number is $>> 1$ and the compression ratio is 4. While $B \geq B_{low}$ is a prerequisite for the incompleteness of the ZA07 model, stronger magnetic fields are required for the ZA07 model to function effectively.

Equation 5.4 from [Tsuji et al. \(2020\)](#) is typically valid as it defines the condition in which the cutoff is restricted by cooling. However, computing B_{low} involves substituting η , which we pre-estimate under the assumption that cooling is the limiting factor, an approach that is not entirely accurate. The B_{low} estimates assume synchrotron cooling limits, which implies that they should be closely examined. For example, refer to the magnetic estimate of Vela Jr. in Table 5.1, which has an error margin of nearly 100%. If the magnetic field falls below the estimates from studies papers, SNRs are most likely not cooling-limited.

5.2 SRCUT Model

5.2.1 Acceleration efficiency for SRCUT model

In the SRCUT model, if the electron spectrum is limited by age rather than synchrotron cooling, it can be approximated with a power-law form that includes an exponential cut-off, represented as:

$$N(E) \propto E^{-2} e^{-E/E_{\max}} \quad (5.5)$$

Here, the spectral index of -2 aligns with expectations for diffusive shock acceleration (DSA) occurring at a strong shock front. The synchrotron emission resulting from this specific electron distribution is effectively described by the `srcut` model in `xspec`. The roll-off frequency of the synchrotron spectrum can be expressed by Equation 2 in [H.E.S.S. Collaboration et al. \(2014\)](#) as follows:

$$\nu_{\text{roll}} = 1.6 \times 10^{16} \left(\frac{E_{\max}}{10 \text{ TeV}} \right)^2 \left(\frac{B}{10 \mu\text{G}} \right) \text{ Hz} \quad (5.6)$$

Expressed in c.g.s units, this becomes:

$$\nu_{\text{roll}} = 6.25 \times 10^{18} E_{\max}^2 B \quad (5.7)$$

Conversely, if age constraints limit E_{\max} , it can be formulated under Bohm-like diffusion as:

$$E_{\max} = \frac{3v_s^2 e B t_{\text{age}}}{20 \eta c} \quad (5.8)$$

And this equation was obtained under the assumption that we equate the acceleration time to the age of an SNR, where v_s is the shock velocity, e is the electron charge, t_{age} denotes the age, and η represents the acceleration efficiency. We substitute this into equation 5.7, the expression for acceleration efficiency becomes:

$$\eta = 0.18 \left(\frac{\nu_{\text{roll}}}{10^{17} \text{ Hz}} \right)^{-1/2} \left(\frac{v_s}{10^8 \text{ cm/s}} \right)^2 \left(\frac{B}{10 \mu\text{G}} \right)^{3/2} \left(\frac{t_{\text{age}}}{1000 \text{ yr}} \right) \quad (5.9)$$

Region	η
G1.9+0.3(E)	2.96 ± 0.46
SN 1987A (whole)	0.09 ± 0.01
RX J1713.7-3946 (NW)	2.30 ± 0.37
HESS J1731-347 (NE)	2.02 ± 1.63
G330.2+1.0 (Whole)	3.42 ± 1.98
RCW 86 (NE)	2.74 ± 1.54
Vela Jr (NW)	1.74 ± 1.05
Tycho	0.66 ± 0.37
Kepler	1.82 ± 0.72
SN 1006 (NE)	6.52 ± 1.91

Table 5.2: Values of η for various sources when $B = 10 \mu\text{G}$

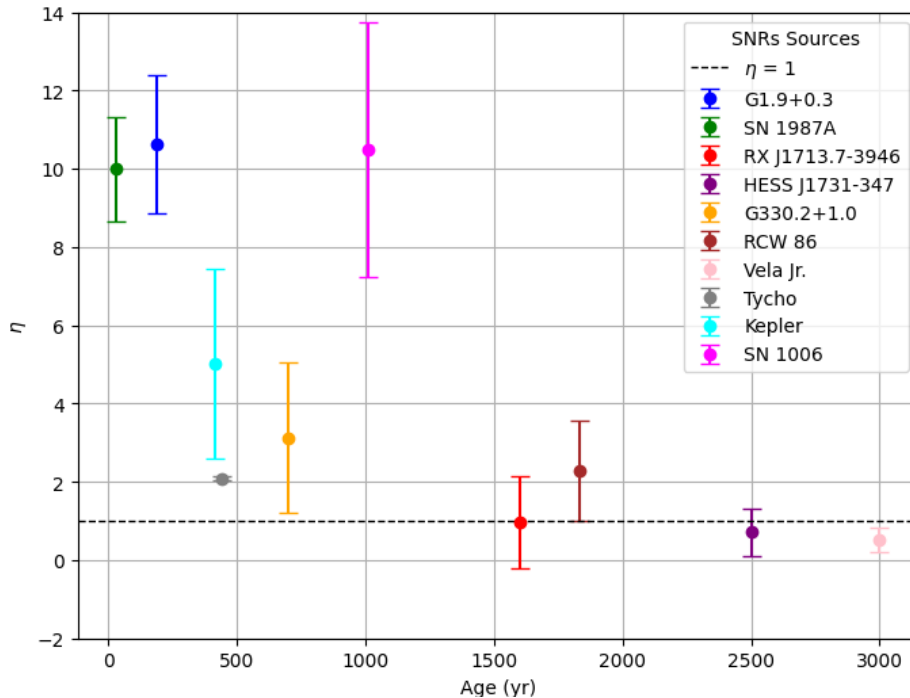
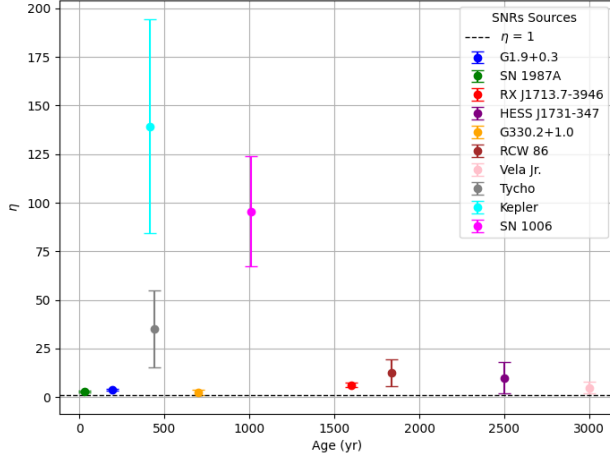


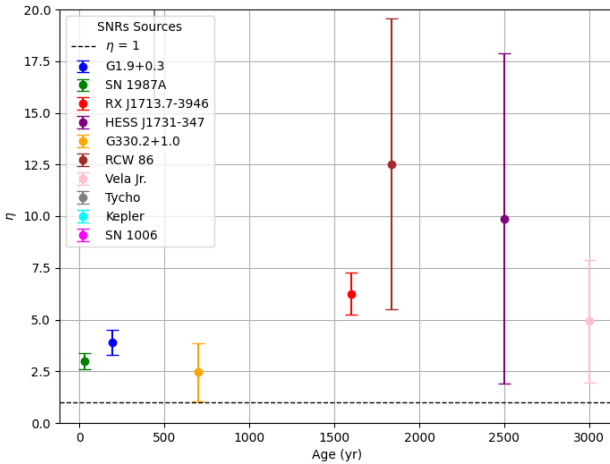
Figure 5.2: Acceleration efficiency against age of SNRs from the SRCUT model, when $B=10 \mu\text{G}$

Figure 5.2 illustrates the relationship between acceleration efficiency and age when applying the baseline magnetic field. Our analysis shows that we are still unable to prove the definition of η as in Tsuji et al. (2020), where they said that all SNRs must have $\eta > 1$. We also explored estimated magnetic fields from existing literature. Refer to Figure 5.3, which provides a comprehensive plot (5.3a) alongside a zoomed-in view (5.3b) to depict all the source variations.

This visual representation supports the way they defined the acceleration efficiency in [Tsui et al. \(2020\)](#), as all SNRs have $\eta > 1$, fixing the problem they had.



(a) Full Plot



(b) Zommed in Plot

Figure 5.3: Acceleration efficiency against age of SNRs from the SRCUT model, when B is different and taken from different papers

5.2.2 Magnetic Estimates for SRCUT model

In many young supernova remnants (SNRs), observations reveal the presence of large, strongly amplified magnetic fields, often much greater than the ambient interstellar medium (ISM) magnetic field strength. Although a $10 \mu\text{G}$ field might be expected purely from compression of the ISM magnetic field, the amplification mechanisms within the SNR shocks lead to significantly stronger fields. These amplified fields suggest efficient particle acceleration processes at work, indicating that magnetic field strengths in young SNRs cannot be solely attributed to compression effects, but rather point to active amplification driven by turbulence and cosmic ray interactions within the shock environment (see [Dickel and Milne \(1976\)](#) for a review).

Since we mentioned that, we also opted for the magnetic field estimates from observational studies and related papers to determine realistic Bohm factors because these field strengths play a critical role in determining particle gyroradii, which in turn influence diffusion and acceleration rates. By incorporating measured or inferred magnetic fields, we can more accurately estimate the Bohm factor (values estimated using equations in 5.2.1, see Table 4.3) that best reflects the physical conditions of the supernova remnant (SNR) environment being modeled. Proper estimates of the magnetic field in supernova remnants (SNRs) play a crucial role in refining calculations of η , the efficiency of cosmic ray acceleration.

Region	Magnetic Field (B , μG)	Acceleration Efficiency (η)
G1.9+0.3 (E)	≈ 12	3.88 ± 0.61
SN 1987A (whole)	10–100	2.98 ± 0.39
RX J1713.7-3946 (NW)	19.5 ± 1.0	6.25 ± 0.1
HESS J1731-347 (NE)	28.8 ± 1.1	9.89 ± 7.97
G330.2+1.0 (Whole)	≈ 8	2.45 ± 1.41
RCW 86 (NE)	27.5 ± 1.1	12.52 ± 7.03
Vela Jr (NW)	≈ 20	4.92 ± 2.96
Tycho	141.3 ± 2.1	35.3 ± 19.81
Kepler	≈ 180	139 ± 55.07
SN 1006 (NE)	60.3 ± 1.1	96.5 ± 28.22

Table 5.3: Magnetic field strengths (B , μG) and acceleration efficiencies (η) for various regions based on SRCUT model parameters. Approximate values are indicated by \approx , and ranges represent observational bounds.

[Sushch et al. \(2018\)](#) estimated the magnetic field strength to be approximately 20 μG (microgauss) in Vela Jr. This magnetic field is obtained from the modeling of the multiwavelength spectral energy distribution from radio to gamma-rays, assuming that gamma-rays are produced via inverse Compton scattering.

In [Ballet \(2006\)](#)'s work on X-ray synchrotron emission from supernova remnants, the magnetic field in the Kepler supernova remnant was estimated to be around 180 μG . This estimation was derived under the assumption that the observed X-ray synchrotron rims are primarily influenced by synchrotron losses, implying rapid electron cooling in high magnetic fields. This field strength was calculated on the basis of the spatial scale of the X-ray emission, with considerations for both diffusion and advection effects on electron transport. Ballet noted that the narrow synchrotron rims in remnants like Kepler suggest strong local magnetic fields necessary to cause significant radiative losses in high-energy electrons behind the shock wave.

In the study of [Zeng et al. \(2019\)](#), they provided magnetic field estimates for several supernova remnants (SNRs), assuming a balanced particle acceleration model and a shock compression factor for accuracy. For RCW 86, HESS J1731-347, and RX J1713.7-3946, they calculated magnetic fields ranging from tens to hundreds of microgauss, with younger remnants like RX J1713.7-3946 showing stronger fields. For SN 1006 and Tycho, they observed relatively moderate magnetic fields due to their older age and differing shock characteristics, indicating varying acceleration dynamics across these SNRs. See Table 5.3 for the estimates obtained.

In the study of [H.E.S.S. Collaboration \(2014\)](#), the magnetic fields of the supernova remnants

were estimated by modeling their multiwavelength emission, particularly the synchrotron X-ray spectra. Assuming a leptonic scenario for γ -ray production and considering synchrotron cooling effects, the magnetic field strength was inferred to be approximately $8.0 \mu\text{G}$ for G330.2+1.0 and $12 \mu\text{G}$ for G1.9+0.3.

Chapter 6

Discussion

6.1 Maximum Attainable Energy

Acceleration efficiency is a critical parameter in estimating the maximum attainable energy of particles in supernova remnants (SNRs). It determines how effectively the energy from shock waves is transferred to accelerate particles, influencing the high-energy cut-off of the spectrum. Efficient acceleration mechanisms, coupled with favorable environmental conditions, such as strong magnetic fields, allow particles to reach higher energies. In contrast, inefficiencies or limitations such as synchrotron cooling or age-related constraints can cap this energy, shaping the observable spectrum and providing insight into the evolutionary stage of the SNR.

Recent studies emphasize the challenge of explaining the "knee" in the cosmic-ray spectrum with supernova remnants (SNRs). Studies consistently show that SNRs struggle to accelerate particles beyond a few hundred TeV, falling short of the PeV range required to explain the knee. See these recent studies ([Marcowith et al., 2018](#); [Cristofari et al., 2020a,b](#); [Inoue et al., 2021](#); [Brose et al., 2022](#); [Diesing, 2023](#)) for a review.

For instance, observations of RX J1713.7-3946 and other SNRs suggest that acceleration efficiency and magnetic field conditions constrain the maximum energies attainable to well below the PeV range. No direct observational evidence supports the SNRs reaching PeV energies under current models (see [Fang et al. \(2022\)](#) and [Angüner et al. \(2023\)](#)). These findings highlight a significant gap in understanding cosmic-ray origins, suggesting that additional mechanisms or sources beyond traditional SNR shock acceleration may be necessary to account for the observed spectrum at higher energies.

For further reading on this topic, you may consult sources like [Vink and Bamba \(2022\)](#) and [Zirakashvili and Aharonian \(2007\)](#) for detailed discussions of particle acceleration in SNRs. I will estimate the maximum attainable energies, checking whether they are limited by cooling or age. I will also discuss the evolution of acceleration efficiency comparing these results with [Tsuji et al. \(2020\)](#).

6.1.1 Equating Synchrotron Cooling Timescale to the Age of a Supernova Remnant

If the synchrotron cooling time for electrons at a certain energy is close to the age of the SNR, it suggests that electrons at this energy are able to exist and radiate over the full duration of the remnant's lifetime. The synchrotron cooling process offers a powerful way to estimate the upper limit on electron energies within a supernova remnant (SNR). As electrons undergo synchrotron radiation in the presence of a magnetic field, their energy gradually decreases over time. The cooling timescale, t_{syn} , for an electron with Lorentz factor γ in a magnetic field B is given by the expression

$$t_{\text{syn}} = \frac{6\pi m_e c}{\sigma_T B^2 \gamma} \quad (6.1)$$

where m_e represents the electron mass, c is the speed of light, σ_T denotes the Thomson cross-section, and B is the magnetic field strength. By equating t_{syn} with the age of the SNR, t_{age} , we can solve the Lorentz factor γ to which the electrons have cooled after this time span, which results in the following results.

$$\gamma = \frac{6\pi m_e c}{\sigma_T B^2 t_{\text{age}}} \quad (6.2)$$

This approach provides the Lorentz factor for electrons that have cooled to this limit within the age of the SNR. Relating this Lorentz factor to the maximum energy retained by the electrons, we find

$$E_{\text{max}} = \gamma m_e c^2 = \frac{6\pi m_e^2 c^3}{\sigma_T B^2 t_{\text{age}}} \quad (6.3)$$

To calculate the maximum synchrotron energy $E_{\text{syn, max}}$, we first determine the maximum synchrotron frequency $\nu_{\text{syn, max}}$ at which the highest energy electrons radiate. The maximum synchrotron frequency depends on the Lorentz factor of the electron γ and the magnetic field B . The synchrotron frequency ν_{syn} for an electron with Lorentz factor γ in a magnetic field B (in Gauss) is given by the expression:

$$\nu_{\text{syn, max}} = \frac{3eB\gamma^2}{2\pi m_e c} \quad (6.4)$$

where:

- e is the elementary charge,
- B is the magnetic field strength in Gauss,
- m_e is the electron mass,

- c is the speed of light.

This equation 6.4 uses the delta-function approximation under the assumption that synchrotron radiation from relativistic electrons is concentrated sharply around a characteristic frequency, simplifying calculations by focusing on this peak emission. However, it should be noted that this approach results in a sharper cutoff in the synchrotron spectrum than observed in reality. In practice, the synchrotron spectrum's high-energy cut-off is more gradual due to the complex distribution of electron energies and magnetic field orientations (see fig. 2 in [Zirakashvili and Aharonian \(2007\)](#)).

Once we have the maximum synchrotron frequency, we can relate it to the maximum synchrotron energy using the equation:

$$E_{\text{syn, max}} = h\nu_{\text{syn, max}} \quad (6.5)$$

where h is Planck's constant. Substituting the expression for $\nu_{\text{syn, max}}$ into this equation gives:

$$E_{\text{syn, max}} = h \left(\frac{3eB\gamma^2}{2\pi m_e c} \right) \quad (6.6)$$

This equation allows me to calculate the energy of the photon radiated by the electron with energy E_{max} . This method allows for the determination of maximum electron energy by assuming that the entire spectrum of accelerated electrons is initially present, subsequently losing energy through cooling over the lifetime of the remnant. If acceleration persists continuously, this energy would correspond to the transition from uncooled to cooled electrons, which would manifest itself as a spectral break in the electron spectrum, with the cutoff occurring at slightly higher energies.

If the maximum synchrotron energy ($E_{\text{syn,max}}$) exceeds the observed cut-off energy, it strongly suggests that the emission of the SNR is not constrained by synchrotron cooling but rather by the age of the SNR. However, when $E_{\text{syn,max}}$ is lower than the observed cut-off energy, it does not definitively indicate a cooling-limited regime. For a confident determination of the cooling limitation, $E_{\text{syn,max}}$ must be significantly lower than the observed cut-off energy. If the two are approximately equal, the cut-off in the X-ray spectrum of the SNR might still be age-limited, as this analysis does not explicitly consider the intricacies of particle acceleration mechanisms.

Findings

In this subsection we discuss the results of the energy estimate when considering that the synchrotron timescale is equal to the age of the SNR. Table 6.1 shows the estimated results for this condition.

From Table 6.1, the analysis of synchrotron emission for selected supernova remnants (SNRs)

SNR Name	$E_{\text{syn,max}}$ (keV)	ϵ_0 (keV)	ϵ_{roll} (keV)	$E_{e,\text{max}}$ (TeV)
G1.9+0.3	167	1.59 ± 0.10	1.59 ± 0.08	88.7
Tycho	0.054	0.299 ± 1.128	0.23 ± 0.02	11.2
Kepler	0.0104	0.655 ± 0.24	0.74 ± 0.35	14.7
G330.2+1.0	41.6	1.564 ± 0.36	1.36 ± 2.34	108
SN 1006	0.0467	0.288 ± 0.03	0.30 ± 0.02	16.8
RX J1713.7-3946	0.55	1.58 ± 0.17	1.50 ± 0.16	69.4
RCW 86	0.149	0.275 ± 0.016	0.24 ± 0.02	24.4
Vela Jr.	0.145	0.773 ± 0.1	0.64 ± 0.05	47.8
HESS J1731-347	0.07	0.886 ± 0.2	0.80 ± 0.16	42.6
SN 1987A	11.6	0.23 ± 0.01	0.72 ± 0.05	11.7

Table 6.1: Synchrotron parameters for selected SNRs, including maximum synchrotron energy, X-ray cutoff energy, roll-off frequency, and maximum electron energy, with $E_{e,\text{max}}$ converted to TeV.

suggests that certain remnants are primarily constrained by either their age or synchrotron cooling. For instance, G1.9+0.3, with a maximum synchrotron energy ($E_{\text{syn,max}}$) of 167 keV and an observed cutoff energy (ϵ_0) of 1.59 ± 0.10 keV, is clearly age-limited. The value of $E_{\text{syn,max}}$ far exceeds ϵ_0 , indicating that synchrotron cooling plays a minimal role in limiting the emission and the age of the remnant is the dominant factor. Similarly, G330.2+1.0 with $E_{\text{syn,max}} = 41.6$ keV and $\epsilon_0 = 1.564 \pm 0.36$ keV, and SN 1987A, with $E_{\text{syn,max}} = 11.6$ keV and $\epsilon_0 = 0.23 \pm 0.01$ keV, are also likely age-limited, as their maximum synchrotron energies exceed the observed cutoffs by a significant margin, again suggesting that cooling effects are not a major constraint.

However, remnants such as Tycho, with $E_{\text{syn,max}} = 0.054$ keV and $\epsilon_0 = 0.299 \pm 1.128$ keV, and Kepler, with $E_{\text{syn,max}} = 0.0104$ keV and $\epsilon_0 = 0.655 \pm 0.24$ keV, show that $E_{\text{syn,max}}$ is much smaller than ϵ_0 , indicating that they are likely cooling-limited. The lower maximum synchrotron energies and the relatively close proximity of the cutoff energies suggest that synchrotron radiation efficiently cooling the particles, limiting the maximum energy before significant loss occurs.

In a similar vein, SN 1006 with $E_{\text{syn,max}} = 0.0467$ keV and $\epsilon_0 = 0.288 \pm 0.03$ keV is also cooling-limited, as $E_{\text{syn,max}}$ is much lower than ϵ_0 . For RX J1713.7-3946, which has $E_{\text{syn,max}} = 0.55$ keV and $\epsilon_0 = 1.58 \pm 0.17$ keV, and Vela Jr. with $E_{\text{syn,max}} = 0.145$ keV and $\epsilon_0 = 0.773 \pm 0.1$ keV, the maximum synchrotron energies are close to the observed cutoffs, indicating that these SNRs are likely age-limited but may still experience some cooling effects, especially considering the uncertainties in the cutoff energies and the smoother, more gradual nature of the synchrotron spectrum. RCW 86, with $E_{\text{syn,max}} = 0.149$ keV and $\epsilon_0 = 0.275 \pm 0.016$ keV, also lies close to the threshold, suggesting that it is age-limited with some possible cooling contributions, as the values of $E_{\text{syn,max}}$ and ϵ_0 are comparable.

Finally, HESS J1731-347, with $E_{\text{syn,max}} = 0.07$ keV and $\epsilon_0 = 0.886 \pm 0.2$ keV, is clearly cooling-limited, as its $E_{\text{syn,max}}$ is significantly lower than ϵ_0 , which implies that synchrotron cooling is the dominant process limiting emission.

Overall, the analysis shows that SNRs like G1.9+0.3, G330.2+1.0, and SN 1987A are primarily age-limited, while Tycho, Kepler, and HESS J1731-347 are more likely cooling-limited, with RX J1713.7-3946, RCW 86, and Vela Jr. representing cases that might involve both processes, but we will consider them age-limited based on their proximity of $E_{\text{syn,max}}$ to ϵ_0 and the uncertainties involved.

6.2 Evolution of η

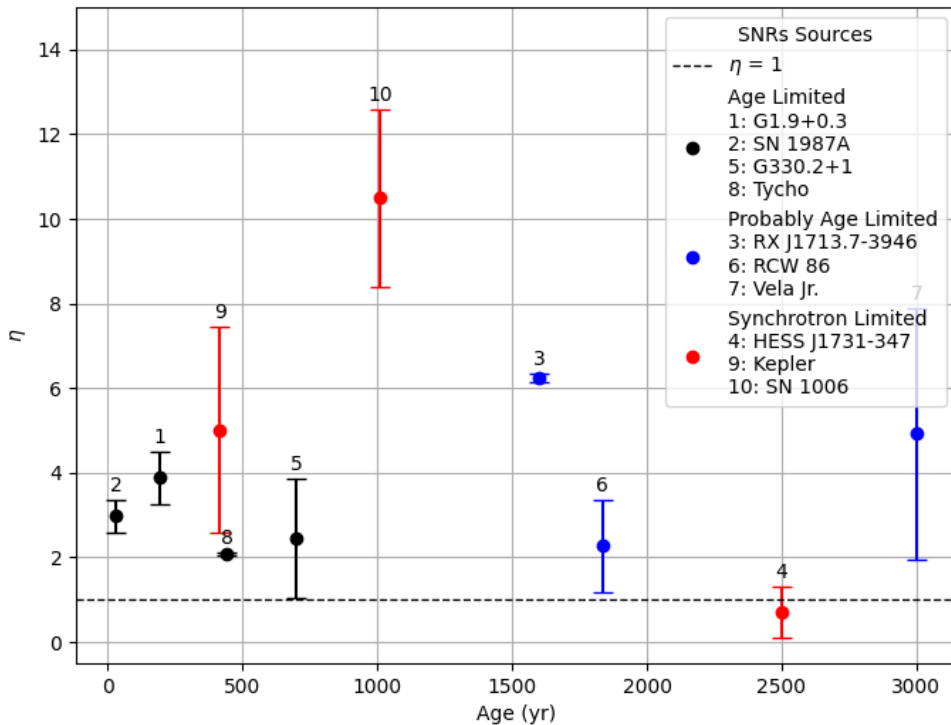


Figure 6.1: Acceleration efficiency against age of SNRs

Figure 6.1 illustrates the acceleration efficiency (η) of cosmic rays in various supernova remnants (SNRs) as a function of their age. For most SNRs, the acceleration efficiency falls between 2 and 5, suggesting a moderate efficiency in cosmic-ray acceleration. In particular, there is no clear dependence of η on the age of the remnant, indicating that the efficiency of cosmic-ray acceleration remains relatively constant over time for the majority of SNRs.

However, two significant outliers are observed:

- **SN 1006:** Shows a much higher value of $\eta \approx 10$.
- **HESS J1731-347:** Shows an ideal $\eta = 1$, corresponding to Bohm diffusion, indicating highly efficient acceleration close to the theoretical maximum.

These observed variations in acceleration efficiency highlight the complexity of the processes occurring in different SNRs and suggest that factors such as shock strength, magnetic field configuration, and environmental conditions play a crucial role in determining the efficiency of cosmic-ray acceleration in SNRs.

[Tsuji et al. \(2020\)](#) proposed a linear evolution of the acceleration efficiency (η) with time. According to their model, η starts at 10 during the early stages of a supernova remnant (SNR) and gradually decreases to 1 as the remnant ages. This implies that the acceleration efficiency improves over time as the remnant ages.

However, in our analysis, we relax the assumption that the cut-off is primarily limited by cooling processes and instead consider the possibility that the maximum energy may be more strongly constrained by the age of the SNR itself. Our findings show that η remains largely constant throughout the age range from 0 to 3000 years, with most SNRs exhibiting values between 2 and 5. This suggests that the acceleration efficiency does not necessarily improve with age, as proposed by [Tsuji et al. \(2020\)](#), but rather stabilizes at a moderate value.

Chapter 7

Conclusions and Outlooks

7.1 Conclusions

In this chapter, we conclude our results by checking whether an SNR is limited by age or cooling. The examination of supernova remnants in Section 6.1 suggests that the synchrotron cooling mechanism significantly constrains the highest energies achieved by accelerated particles. We conducted an analysis of X-ray data from 10 young supernova remnants (SNRs) to identify the cut-off energy parameter in the synchrotron spectrum, which allowed us to constrain the Bohm factor for each SNR.

From our results in Section 6.1, the analysis of synchrotron emission from selected supernova remnants (SNRs) suggests that the emission mechanisms in these remnants are primarily governed by either the age of the remnant or synchrotron cooling, with some remnants exhibiting characteristics of both.

Comparing Maximum Energy Estimates

Remnants such as **G1.9+0.3**, **G330.2+1.0**, and **SN 1987A** are predominantly age-limited, as evidenced by their maximum synchrotron energies significantly exceeding the observed cut-off energies. This suggests that synchrotron cooling is not the limiting factor, and particle acceleration remains the dominant process.

In contrast, remnants like **Tycho**, **Kepler**, and **HESS J1731-347** are cooling-limited. Their maximum synchrotron energies are much lower than their observed cutoff energies, indicating that synchrotron radiation effectively cooling the particles before they can reach higher energies.

SNRs such as **RX J1713.7-3946**, **RCW 86**, and **Vela Jr.**, which have maximum synchrotron energies close to their observed cut-offs, are considered most probably age-limited. The electron spectrum is not expected to be significantly modified by cooling and hence SRCUT model is more appropriate to fit the X-ray spectrum.

These findings underscore the complexity of SNR emission, where the age of the remnant is the dominant factor for most, while cooling plays a crucial role in others. This highlights the need for further detailed modeling to refine our understanding of particle acceleration and energy loss mechanisms in these fascinating cosmic objects.

Evolution of the Acceleration Efficiency with Time

Taking into account the 10 supernova remnants (SNRs) such as G330.2+1.0, RX J1713.7-3946, RCW 86, Vela Jr., HESS J1731-347 and SN 1987A, the systematic pattern of the Bohm factor has been identified in our study after it was reported in [Tsugi et al. \(2020\)](#). Relaxing the condition that maximum electron energies are limited by synchrotron cooling and taking into account that the maximum energy could be also limited by the age of SNRs suggests that the acceleration efficiency remains in the range $\eta \sim 2 - 6$ during first ~ 3000 years of evolution (based on the ages of considered SNRs). This suggests that, contrary to the linear evolution model proposed by [Tsugi et al. \(2020\)](#), the acceleration efficiency does not necessarily improve with time, but rather operates at the same level.

The observed outliers, SN 1006 with a high $\eta \approx 10$ and HESS J1731-347 with $\eta \approx 1$ further emphasize the complexity of cosmic ray acceleration in SNRs. In particular, it is intriguing that HESS J1731-347 seems to operate in the mode of ideal Bohm diffusion with particularly effective particle acceleration.

7.2 Outlooks

The findings from this study of supernova remnants (SNRs) provide important insights into the processes of particle acceleration and cooling in astrophysical settings. Looking ahead, I intend to conduct statistical analyses to assess whether there is any notable temporal variation in the acceleration efficiency across the ages being considered. This knowledge can facilitate the development of models that accurately forecast the behavior of cosmic rays and their origins.

Furthermore, I plan to incorporate gamma-ray data in future analysis, which could (if leptonic in nature) offer direct estimates of maximum electron energies and significantly assist the study. Notably, some of these remnants are currently undetected in gamma-rays, and it should be mentioned that the future CTA may address this.

Bibliography

- Abdalla, H., Abramowski, A., Aharonian, F., Benkhali, F. A., Angüner, E., Arakawa, M., Arrieta, M., Aubert, P., Backes, M., Balzer, A., et al. (2018). Population study of galactic supernova remnants at very high γ -ray energies with hess. *Astronomy & Astrophysics*, 612:A3.
- Abramowski, A., Acero, F., Aharonian, F., Akhperjanian, A., Anton, G., Balzer, A., Barnacka, A., De Almeida, U. B., Becherini, Y., Becker, J., et al. (2011). A new snr with tev shell-type morphology: Hess j1731-347. *Astronomy & Astrophysics*, 531:A81.
- Acero, F., Ackermann, M., Ajello, M., Albert, A., Atwood, W., Axelsson, M., Baldini, L., Ballet, J., Barbiellini, G., Bastieri, D., et al. (2015). Fermi large area telescope third source catalog. *The Astrophysical Journal Supplement Series*, 218(2):23.
- Acero, F., Ackermann, M., Ajello, M., Baldini, L., Ballet, J., Barbiellini, G., Bastieri, D., Bellazzini, R., Bissaldi, E., Blandford, R., et al. (2016). The first fermi-lat supernova remnant catalog. *The Astrophysical Journal Supplement Series*, 224(1):8.
- Acero, F., Katsuda, S., Ballet, J., and Petre, R. (2017). Measurement of the x-ray proper motion in the south-east rim of rx j1713. 7- 3946. *Astronomy & Astrophysics*, 597:A106.
- Ackermann, M., Ajello, M., Allafort, A., Baldini, L., Ballet, J., Barbiellini, G., Baring, M., Bastieri, D., Bechtol, K., Bellazzini, R., et al. (2013). Detection of the characteristic pion-decay signature in supernova remnants. *Science*, 339(6121):807–811.
- Aharonian, F., Akhperjanian, A., Aye, K.-M., Bazer-Bachi, A., Beilicke, M., Benbow, W., Berge, D., Berghaus, P., Bernlöhr, K., Bolz, O., et al. (2004). High-energy particle acceleration in the shell of a supernova remnant. *Nature*, 432(7013):75–77.
- Aharonian, F., Akhperjanian, A., Barrio, J., Bernlöhr, K., Börst, H., Bojahr, H., Bolz, O., Contreras, J., Cortina, J., Denninghoff, S., et al. (2001). Evidence for tev gamma ray emission from cassiopeia a. *Astronomy & Astrophysics*, 370(1):112–120.
- Aharonian, F. and Atoyan, A. (1999). On the origin of tev radiation of sn 1006. *arXiv preprint astro-ph/9911158*.
- Aharonian, F., Barkov, M., and Khangulyan, D. (2017). Scenarios for ultrafast gamma-ray variability in agn. *The Astrophysical Journal*, 841(1):61.
- Ahnen, M. L., Ansoldi, S., Antonelli, L., Arcaro, C., Babić, A., Banerjee, B., Bangale, P., Barres de Almeida, U., Barrio, J., Becerra González, J., et al. (2017). A cut-off in the tev

- gamma-ray spectrum of the snr cassiopeia a. *Monthly Notices of the Royal Astronomical Society*, 472(3):2956–2962.
- Allen, G. E., Chow, K., DeLaney, T., Filipović, M., Houck, J. C., Pannuti, T. G., and Stage, M. D. (2014). On the expansion rate, age, and distance of the supernova remnant g266. 2-1.2 (vela jr.). *The Astrophysical Journal*, 798(2):82.
- Anderson, L., Camilo, F., Faerber, T., Bietenholz, M., Bordiu, C., Bufano, F., Chibueze, J., Cotton, W., Ingallinera, A., Loru, S., et al. (2024). Supernova remnant candidates discovered by the sarao meerkat galactic plane survey. *arXiv preprint arXiv:2409.16607*.
- Angüner, E. O., Spengler, G., Amato, E., and Casanova, S. (2023). Search for the galactic accelerators of cosmic rays up to the knee with the pevatron test statistic. *Monthly Notices of the Royal Astronomical Society*, 523(3):4097–4112.
- Archambault, S., Archer, A., Benbow, W., Bird, R., Bourbeau, E., Buchovecky, M., Buckley, J., Bugaev, V., Cerruti, M., Connolly, M., et al. (2017). Gamma-ray observations of tycho's supernova remnant with veritas and fermi. *The Astrophysical Journal*, 836(1):23.
- Arnett, D. (1996). *Supernovae and nucleosynthesis: an investigation of the history of matter, from the big bang to the present*. Princeton University Press.
- Ballet, J. (2006). X-ray synchrotron emission from supernova remnants. *Advances in Space Research*, 37(10):1902–1908.
- Beringer, J., Arguin, J., Barnett, R., Copic, K., Dahl, O., Groom, D., Lin, C., Lys, J., Murrayama, H., Wohl, C., et al. (2012). Review of particle physics. *Physical Review D*, 86(1).
- Bionta, R., Blewitt, G., Bratton, C., Casper, D., Ciocio, A., Claus, R., Cortez, B., Crouch, M., Dye, S., Errede, S., et al. (1987). Observation of a neutrino burst in coincidence with supernova 1987a in the large magellanic cloud. *Physical Review Letters*, 58(14):1494.
- Blondin, J. M. and Mezzacappa, A. (2007). Pulsar spins from an instability in the accretion shock of supernovae. *Nature*, 445(7123):58–60.
- Blondin, J. M., Mezzacappa, A., and DeMarino, C. (2003). Stability of standing accretion shocks, with an eye toward core-collapse supernovae. *The Astrophysical Journal*, 584(2):971.
- Blumenthal, G. R. and Gould, R. J. (1970). Bremsstrahlung, synchrotron radiation, and compton scattering of high-energy electrons traversing dilute gases. *Reviews of modern Physics*, 42(2):237.
- Borkowski, K. J., Gwynne, P., Reynolds, S. P., Green, D. A., Hwang, U., Petre, R., and Willett, R. (2017). Asymmetric expansion of the youngest galactic supernova remnant g1. 9+ 0.3. *The Astrophysical Journal Letters*, 837(1):L7.
- Borkowski, K. J., Reynolds, S. P., Hwang, U., Green, D. A., Petre, R., Krishnamurthy, K., and Willett, R. (2013). Supernova ejecta in the youngest galactic supernova remnant g1. 9+ 0.3. *The Astrophysical Journal Letters*, 771(1):L9.

- Branch, D., Buta, R., Falk, S., Lccall, M., Sutherland, P., Uomoto, A., Wheeler, J., and Wills, B. (1982). Interpretation of the maximum light spectrum of a type i supernova. *Astrophysical Journal, Part 2-Letters to the Editor, vol. 252, Jan. 15, 1982, p. L61-L64. Research supported by the Natural Sciences and Engineering Research Council of Canada*, 252:L61–L64.
- Brose, R., Sushch, I., and Mackey, J. (2022). Core-collapse supernovae in dense environments - particle acceleration and non-thermal emission. , 516(1):492–505.
- Burrows, A., Dessart, L., Livne, E., Ott, C. D., and Murphy, J. (2007). Simulations of magnetically driven supernova and hypernova explosions in the context of rapid rotation. *The Astrophysical Journal*, 664(1):416.
- Cassam-Chenaï, G., Decourchelle, A., Ballet, J., Sauvageot, J.-L., Dubner, G., and Giacani, E. (2004). Xmm-newton observations of the supernova remnant rx j1713. 7–3946 and its central source. *Astronomy & Astrophysics*, 427(1):199–216.
- Cesur, N., Sezer, A., and HÜDAVERDİ, M. (2018). Spectral properties of the galactic supernova remnant vela jr.(g266. 2-1.2) using chandra. *Turkish Journal of Physics*, 42(2):166–174.
- Chevalier, R. A. (1974). The evolution of supernova remnants. spherically symmetric models. *Astrophysical Journal, Vol. 188, pp. 501-516 (1974)*, 188:501–516.
- Chevalier, R. A. (2005). Young core-collapse supernova remnants and their supernovae. *The Astrophysical Journal*, 619(2):839.
- Chieffi, A. and Limongi, M. (2004). Explosive yields of massive stars from $z= 0$ to $z= z$. *The Astrophysical Journal*, 608(1):405.
- Cristofari, P., Blasi, P., and Amato, E. (2020a). The low rate of Galactic pevatrons. *Astroparticle Physics*, 123:102492.
- Cristofari, P., Renaud, M., Marcowith, A., Dwarkadas, V. V., and Tatischeff, V. (2020b). Time-dependent high-energy gamma-ray signal from accelerated particles in core-collapse supernovae: the case of SN 1993J. , 494(2):2760–2765.
- Dermer, C. (1986). Secondary production of neutral pi-mesons and the diffuse galactic gamma radiation. *Astronomy and Astrophysics (ISSN 0004-6361), vol. 157, no. 2, March 1986, p. 223-229.*, 157:223–229.
- Dermer, C., Finke, J., Murphy, R., Strong, A., Loparco, F., Mazziotta, M., Orlando, E., Kamae, T., Tibaldo, L., Cohen-Tanugi, J., et al. (2013). On the physics connecting cosmic rays and gamma rays: Towards determining the interstellar cosmic ray spectrum. *arXiv preprint arXiv:1303.6482*.
- Dickel, J. R. and Milne, D. (1976). Magnetic fields in supernova remnants. *Australian Journal of Physics, vol. 29, Oct. 1976, p. 435-460.*, 29:435–460.
- Diesing, R. (2023). The Maximum Energy of Shock-accelerated Cosmic Rays. , 958(1):3.

- Drury, L. (1983). On particle acceleration in supernova remnants. In *Galactic Astrophysics and Gamma-Ray Astronomy: Proceedings of a Meeting Organised in the Context of the XVIII General Assembly of the IAU, held in Patras, Greece, August 19, 1982*, pages 57–60. Springer.
- Elias, J., Matthews, K., Neugebauer, G., and Persson, S. (1985). Type i supernovae in the infrared and their use as distance indicators. *Astrophysical Journal*, 296:379–389.
- Fang, K., Kerr, M., Blandford, R., Fleischhack, H., and Charles, E. (2022). Evidence for pev proton acceleration from fermi-lat observations of snr G106.3 + 2.7. *Phys. Rev. Lett.*, 129:071101.
- Federici, S., Pohl, M., Telezhinsky, I., Wilhelm, A., and Dwarkadas, V. (2015). Analysis of gev-band γ -ray emission from supernova remnant rx j1713. 7-3946. *Astronomy & Astrophysics*, 577:A12.
- Frank, K. A., Zhekov, S. A., Park, S., McCray, R., Dwek, E., and Burrows, D. N. (2016). Chandra observes the end of an era in sn 1987a. *The Astrophysical Journal*, 829(1):40.
- Galama, T. J., Vreeswijk, P., Van Paradijs, J., Kouveliotou, C., Augusteijn, T., Böhnhardt, H., Brewer, J., Doublier, V., Gonzalez, J.-F., Leibundgut, B., et al. (1998). An unusual supernova in the error box of the γ -ray burst of 25 april 1998. *nature*, 395(6703):670–672.
- Garnavich, P. M., Jha, S., Challis, P., Clocchiatti, A., Diercks, A., Filippenko, A. V., Gilliland, R. L., Hogan, C. J., Kirshner, R. P., Leibundgut, B., et al. (1998). Supernova limits on the cosmic equation of state. *The Astrophysical Journal*, 509(1):74.
- Garrel, C., Vlahos, L., Isliker, H., and Pisokas, T. (2018). Diffusive shock acceleration and turbulent reconnection. *Monthly Notices of the Royal Astronomical Society*, 478(3):2976–2986.
- Ginzburg, V. L. and Syrovatskii, S. (1965). Cosmic magnetobremssstrahlung (synchrotron radiation). *Annual Review of Astronomy and Astrophysics*, 3(1):297–350.
- Ginzburg, Vitalii L and Syrovatskiĭ, S. (1966). Cosmic magnetic bremsstrahlung (synchrotron radiation). *Soviet Physics Uspekhi*, 8(5):674.
- Gould, R. J. (1975). Energy loss of relativistic electrons and positrons traversing cosmic matter. *Astrophysical Journal*, vol. 196, Mar. 15, 1975, pt. 1, p. 689-694. Research supported by the Alfred P. Sloan Foundation;, 196:689–694.
- Green, D. A. (2009). A revised galactic supernova remnant catalogue. *arXiv preprint arXiv:0905.3699*.
- Hachisu, I., Kato, M., and Nomoto, K. (1999). A wide symbiotic channel to type ia supernovae. *The Astrophysical Journal*, 522(1):487.
- Hamuy, M., Phillips, M., Suntzeff, N. B., Maza, J., González, L., Roth, M., Krisciunas, K., Morrell, N., Green, E., Persson, S., et al. (2003). An asymptotic-giant-branch star in the progenitor system of a type ia supernova. *Nature*, 424(6949):651–654.

- Harkness, R. P. and Wheeler, J. C. (1990). Classification of supernovae. In *Supernovae*, pages 1–29. Springer.
- Heger, A., Fryer, C. L., Woosley, S. E., Langer, N., and Hartmann, D. H. (2003). How massive single stars end their life. *The Astrophysical Journal*, 591(1):288.
- H.E.S.S. Collaboration (2014). Tev γ -ray observations of the young synchrotron-dominated snrs g1. 9+ 0.3 and g330. 2+ 1.0 with hess. *Monthly Notices of the Royal Astronomical Society*, 441(1):790–799.
- Hirata, K., Kajita, T., Koshiba, M., Nakahata, M., Oyama, Y., Sato, N., Suzuki, A., Takita, M., Totsuka, Y., Kifune, T., et al. (1987). Observation of a neutrino burst from the supernova sn1987a. *Physical Review Letters*, 58(14):1490.
- Inoue, T., Marcowith, A., Giacinti, G., Jan van Marle, A., and Nishino, S. (2021). Direct Numerical Simulations of Cosmic-ray Acceleration at Dense Circumstellar Medium: Magnetic-field Amplification and Maximum Energy. , 922(1):7.
- Iwamoto, K., Brachwitz, F., Nomoto, K., Kishimoto, N., Umeda, H., Hix, W. R., and Thielemann, F.-K. (1999). Nucleosynthesis in chandrasekhar mass models for type ia supernovae and constraints on progenitor systems and burning-front propagation. *The Astrophysical Journal Supplement Series*, 125(2):439.
- Janka, H.-T., Langanke, K., Marek, A., Martínez-Pinedo, G., and Müller, B. (2007). Theory of core-collapse supernovae. *Physics Reports*, 442(1-6):38–74.
- Jones, F. C. (1968). Calculated spectrum of inverse-compton-scattered photons. *Physical Review*, 167(5):1159.
- Kalberla, P. M., Burton, W., Hartmann, D., Arnal, E. M., Bajaja, E., Morras, R., and Pöppel, W. G. (2005). The leiden/argentine/bonn (lab) survey of galactic hi-final data release of the combined lds and iar surveys with improved stray-radiation corrections. *Astronomy & Astrophysics*, 440(2):775–782.
- Katsuda, S., Tsunemi, H., Uchida, H., and Kimura, M. (2008). Forward shock proper motions of kepler's supernova remnant. *The Astrophysical Journal*, 689(1):225.
- Kelly, P. L., Kirshner, R. P., and Pahre, M. (2008). Long γ -ray bursts and type ic core-collapse supernovae have similar locations in hosts. *The Astrophysical Journal*, 687(2):1201.
- Khokhlov, A. (1991). Delayed detonation model for type ia supernovae. *Astronomy and Astrophysics (ISSN 0004-6361)*, vol. 245, no. 1, May 1991, p. 114-128., 245:114–128.
- Koyama, K., Petre, R., Gotthelf, E., Hwang, U., Matsuura, M., Ozaki, M., and Holt, S. (1995). Evidence for shock acceleration of high-energy electrons in the supernova remnant sn1006. *Nature*, 378(6554):255–258.
- Krause, O., Birkmann, S. M., Usuda, T., Hattori, T., Goto, M., Rieke, G. H., and Misselt, K. A. (2008). The cassiopeia a supernova was of type iib. *Science*, 320(5880):1195–1197.

- Lazarevich, G. and Syrovatskii, S. I. (2013). *The origin of cosmic rays*. Elsevier.
- Li, J.-T., Ballet, J., Miceli, M., Zhou, P., Vink, J., Chen, Y., Acero, F., Decourchelle, A., and Bregman, J. N. (2018). Spatially resolved broadband synchrotron emission from the nonthermal limbs of sn1006. *The Astrophysical Journal*, 864(1):85.
- Longair, M. (2011). High energy astrophysics (3rd edn; cambridge).
- Marcowith, A., Dwarkadas, V. V., Renaud, M., Tatischeff, V., and Giacinti, G. (2018). Core-collapse supernovae as cosmic ray sources. , 479(4):4470–4485.
- Mazzali, P. A., Ropke, F. K., Benetti, S., and Hillebrandt, W. (2007). A common explosion mechanism for type ia supernovae. *Science*, 315(5813):825–828.
- Merloni, A., Lamer, G., Liu, T., Ramos-Ceja, M., Brunner, H., Bulbul, E., Dennerl, K., Doroshenko, V., Freyberg, M., Friedrich, S., et al. (2024). The srg/erosita all-sky survey-first x-ray catalogues and data release of the western galactic hemisphere. *Astronomy & Astrophysics*, 682:A34.
- Miceli, M., Bocchino, F., Iakubovskyi, D., Orlando, S., Telezhinsky, I., Kirsch, M., Petruk, O., Dubner, G., and Castelletti, G. (2009). Thermal emission, shock modification, and x-ray emitting ejecta in sn 1006. *Astronomy & Astrophysics*, 501(1):239–249.
- Michailidis, M., Pühlhofer, G., Becker, W., Freyberg, M., Merloni, A., Santangelo, A., Sasaki, M., Bykov, A., Chugai, N., Churazov, E., et al. (2024). Study of x-ray emission from the s147 nebula with srg/erosita: X-ray imaging, spectral characterization and a multiwavelength picture. *arXiv preprint arXiv:2401.17312*.
- Minkowski, R. (1964). Supernovae and supernova remnants. *Annual Review of Astronomy and Astrophysics*, 2(1):247–266.
- Nomoto, K. (1982). Accreting white dwarf models for type i supernovae. i-presupernova evolution and triggering mechanisms. *Astrophysical Journal, Part 1*, vol. 253, Feb. 15, 1982, p. 798-810., 253:798–810.
- Pacholczyk, A. (1970). Non thermal processes in galactic and extragalactic sources. *Radio Astrophysics*.
- Park, S., Mori, K., Kargaltsev, O., Slane, P. O., Hughes, J. P., Burrows, D. N., Garmire, G. P., and Pavlov, G. G. (2006). Discovery of a candidate central compact object in the galactic nonthermal snr g330. 2+ 1.0. *The Astrophysical Journal*, 653(1):L37.
- Perlmutter, S., Aldering, G., Valle, M. D., Deustua, S., Ellis, R., Fabbro, S., Fruchter, A., Goldhaber, G., Groom, D., Hook, I., et al. (1998). Discovery of a supernova explosion at half the age of the universe. *Nature*, 391(6662):51–54.
- Phillips, M. M., Wells, L. A., Suntzeff, N. B., Hamuy, M., Leibundgut, B., Kirshner, R. P., and Foltz, C. B. (1992). Sn 1991t-further evidence of the heterogeneous nature of type ia supernovae. *Astronomical Journal (ISSN 0004-6256)*, vol. 103, no. 5, May 1992, p. 1632-1637, 1718., 103:1632–1637.

- Podsiadlowski, P., Hsu, J., Joss, P., and Ross, R. (1993). The progenitor of supernova 1993j: a stripped supergiant in a binary system? *Nature*, 364(6437):509–511.
- Podsiadlowski, P., Joss, P., and Hsu, J. (1992). Presupernova evolution in massive interacting binaries. *Astrophysical Journal, Part 1 (ISSN 0004-637X)*, vol. 391, no. 1, May 20, 1992, p. 246-264., 391:246–264.
- Pohl, M., Yan, H., and Lazarian, A. (2005). Magnetically limited x-ray filaments in young supernova remnants. *The Astrophysical Journal*, 626(2):L101.
- Porter, T. A., Moskalenko, I. V., and Strong, A. W. (2006). Inverse compton emission from galactic supernova remnants: effect of the interstellar radiation field. *The Astrophysical Journal*, 648(1):L29.
- Rankine, W. J. M. (1870). Xv. on the thermodynamic theory of waves of finite longitudinal disturbance. *Philosophical Transactions of the Royal Society of London*, (160):277–288.
- Reynolds, S. P. (1998). Models of synchrotron x-rays from shell supernova remnants. *The Astrophysical Journal*, 493(1):375.
- Reynolds, S. P. (2008). Supernova remnants at high energy. *Annu. Rev. Astron. Astrophys.*, 46:89–126.
- Reynolds, S. P. and Ellison, D. C. (1992). Electron acceleration in tycho's and kepler's supernova remnants-spectral evidence of fermi shock acceleration. *Astrophysical Journal, Part 2-Letters (ISSN 0004-637X)*, vol. 399, no. 1, p. L75-L78., 399:L75–L78.
- Riess, A. G., Strolger, L.-G., Casertano, S., Ferguson, H. C., Mobasher, B., Gold, B., Challis, P. J., Filippenko, A. V., Jha, S., Li, W., et al. (2007). New hubble space telescope discoveries of type ia supernovae at z 1: narrowing constraints on the early behavior of dark energy. *The Astrophysical Journal*, 659(1):98.
- Ruiter, A. J., Belczynski, K., and Fryer, C. (2009). Rates and delay times of type ia supernovae. *The Astrophysical Journal*, 699(2):2026.
- Rybicki, G. B. and Lightman, A. P. (1991). *Radiative processes in astrophysics*. John Wiley & Sons.
- Sato, T., Katsuda, S., Morii, M., Bamba, A., Hughes, J. P., Maeda, Y., Ishida, M., and Fraschetti, F. (2018). X-ray measurements of the particle acceleration properties at inward shocks in cassiopeia a. *The Astrophysical Journal*, 853(1):46.
- Sedov, L. I. (2018). *Similarity and dimensional methods in mechanics*. CRC press.
- Sedov, L. I., Friedman, M., Holt, M., and Cole, J. (1959). Similarity and dimensional methods in mechanics. *The Astrophysical Journal*.
- Shen, K. J. and Bildsten, L. (2007). Thermally stable nuclear burning on accreting white dwarfs. *The Astrophysical Journal*, 660(2):1444.

- Shklovskii, I. (1953). The problem of cosmic radioemission.< title lang="ru"> problema kosmicheskogo radioizlucheniâ. *Astronomicheskii Zhurnal*, 30:15–36.
- Slane, P., Gaensler, B. M., Dame, T., Hughes, J. P., Plucinsky, P. P., and Green, A. (1999). Nonthermal x-ray emission from the shell-type supernova remnant g347. 3–0.5. *The Astrophysical Journal*, 525(1):357.
- Smartt, S. J. (2009). Progenitors of core-collapse supernovae. *Annual Review of Astronomy and Astrophysics*, 47:63–106.
- Stanek, K. Z., Matheson, T., Garnavich, P., Martini, P., Berlind, P., Caldwell, N., Challis, P., Brown, W., Schild, R., Krisciunas, K., et al. (2003). Spectroscopic discovery of the supernova 2003dh associated with grb 030329. *The Astrophysical Journal*, 591(1):L17.
- Stecker, F. W. (1971). *Cosmic gamma rays*, volume 249. Scientific and Technical Information Office, National Aeronautics and Space
- Stephenson, F. R., Clark, D. H., and Crawford, D. F. (1977). The supernova of ad 1006. *Monthly Notices of the Royal Astronomical Society*, 180(4):567–584.
- Sushch, I., Brose, R., and Pohl, M. (2018). Modeling of the spatially resolved nonthermal emission from the vela jr. supernova remnant. *Astronomy & Astrophysics*, 618:A155.
- Tanaka, T., Uchiyama, Y., Aharonian, F. A., Takahashi, T., Bamba, A., Hiraga, J. S., Kataoka, J., Kishishita, T., Kokubun, M., Mori, K., et al. (2008). Study of nonthermal emission from snr rx j1713. 7–3946 with suzaku. *The Astrophysical Journal*, 685(2):988.
- Taylor, G. I. (1950). The formation of a blast wave by a very intense explosion i. theoretical discussion. *Proceedings of the Royal Society of London. Series A. Mathematical and Physical Sciences*, 201(1065):159–174.
- Thielemann, F.-K., Nomoto, K., and Hashimoto, M.-A. (1996). Core-collapse supernovae and their ejecta. *Astrophysical Journal* v. 460, p. 408, 460:408.
- Truelove, J. K. and McKee, C. F. (1999). Evolution of nonradiative supernova remnants. *The Astrophysical Journal Supplement Series*, 120(2):299.
- Tsubone, Y., Sawada, M., Bamba, A., Katsuda, S., and Vink, J. (2017). A systematic study of the thermal and nonthermal emission in the supernova remnant rcw 86 with suzaku. *The Astrophysical Journal*, 835(1):34.
- Tsuji, N., Uchiyama, Y., Aharonian, F., Berge, D., Higurashi, R., Krivonos, R., and Tanaka, T. (2019). Nustar observations of the supernova remnant rx j1713. 7–3946. *The Astrophysical Journal*, 877(2):96.
- Tsuji, N., Uchiyama, Y., Khangulyan, D., and Aharonian, F. (2020). Systematic study of acceleration efficiency in young supernova remnants with nonthermal x-ray observations. *The Astrophysical Journal*, 907:117 (21pp), 2021 February 1, 907(2):117.

- Urošević, D. (2014). On the radio spectra of supernova remnants. *Astrophysics and Space Science*, 354:541–552.
- Vink, J. and Bamba, A. (2022). Nonthermal processes and particle acceleration in supernova remnants. In *Handbook of X-ray and Gamma-ray Astrophysics*, pages 1–33. Springer.
- Vink, J. and Laming, J. M. (2003). On the magnetic fields and particle acceleration in cassiopeia a. *The Astrophysical Journal*, 584(2):758.
- Webb, G., Drury, L., and Biermann, P. (1984). Diffusive shock acceleration of energetic electrons subject to synchrotron losses. *Astronomy and Astrophysics (ISSN 0004-6361)*, vol. 137, no. 2, Aug. 1984, p. 185-201., 137:185–201.
- Weinberg, N. N. and Quataert, E. (2008). Non-linear saturation of g-modes in proto-neutron stars: quieting the acoustic engine. *Monthly Notices of the Royal Astronomical Society: Letters*, 387(1):L64–L68.
- Wheeler, J. C., Meier, D. L., and Wilson, J. R. (2002). Asymmetric supernovae from magnetocentrifugal jets. *The Astrophysical Journal*, 568(2):807.
- Williams, B. J., Borkowski, K. J., Ghavamian, P., Hewitt, J. W., Mao, S. A., Petre, R., Reynolds, S. P., and Blondin, J. M. (2013). Azimuthal density variations around the rim of tycho's supernova remnant. *The Astrophysical Journal*, 770(2):129.
- Winkler, P. F., Williams, B. J., Reynolds, S. P., Petre, R., Long, K. S., Katsuda, S., and Hwang, U. (2014). A high-resolution x-ray and optical study of sn 1006: asymmetric expansion and small-scale structure in a type ia supernova remnant. *The Astrophysical Journal*, 781(2):65.
- Woltjer, L. (1972). Supernova remnants. *Annual Review of Astronomy and Astrophysics*, 10(1):129–158.
- Woosley, S., Eastman, R. G., Weaver, T. A., and Pinto, P. A. (1994). Sn 1993j: a type iib supernova. *The Astrophysical Journal, Part 1 (ISSN 0004-637X)*, vol. 429, no. 1, p. 300-318, 429:300–318.
- Woosley, S. and Janka, T. (2005). The physics of core-collapse supernovae. *Nature Physics*, 1(3):147–154.
- Woosley, S., Kasen, D., Blinnikov, S., and Sorokina, E. (2007). Type ia supernova light curves. *The Astrophysical Journal*, 662(1):487.
- Woosley, S. and Weaver, T. A. (1995). The evolution and explosion of massive stars ii: Explosive hydrodynamics and nucleosynthesis. Technical report, Lawrence Livermore National Lab.(LLNL), Livermore, CA (United States).
- Yamaguchi, H., Katsuda, S., Castro, D., Williams, B. J., Lopez, L. A., Slane, P. O., Smith, R. K., and Petre, R. (2016). The refined shock velocity of the x-ray filaments in the rcw 86 northeast rim. *The Astrophysical Journal Letters*, 820(1):L3.

- Zeng, H., Xin, Y., and Liu, S. (2019). Evolution of High-energy Particle Distribution in Supernova Remnants. , 874(1):50.
- Zirakashvili, V. and Aharonian, F. (2007). Analytical solutions for energy spectra of electrons accelerated by nonrelativistic shock-waves in shell type supernova remnants. *Astronomy & Astrophysics*, 465(3):695–702.

Appendix A

DataSet

The data sets of achival observations of Chandra and NuSTAR are listed in Tables [A.1](#) and [A.2](#), respectively.

Table A.1: Table Log for Chandra Observations

Name	Obs ID	Effective Time (ks)	Date	R.A. (deg)	Decl. (deg)
G1.9+0.3	6708	23.9	2007-02-10	267.2	-27.2
G1.9+0.3	8521	25.7	2007-03-03	267.2	-27.2
G1.9+0.3	10111	68.3	2009-07-23	267.2	-27.2
G1.9+0.3	10112	50.8	2009-07-18	267.2	-27.2
G1.9+0.3	10928	35.4	2009-07-13	267.2	-27.2
G1.9+0.3	10930	82.1	2009-07-26	267.2	-27.2
G1.9+0.3	12689	155.6	2011-07-14	267.2	-27.2
G1.9+0.3	12690	48.2	2011-05-16	267.2	-27.2
G1.9+0.3	12691	184.0	2011-05-09	267.2	-27.2
G1.9+0.3	12692	162.6	2011-05-12	267.2	-27.2
G1.9+0.3	12693	127.5	2011-05-18	267.2	-27.2
G1.9+0.3	12694	159.3	2011-05-20	267.2	-27.2
G1.9+0.3	12695	39.5	2011-05-23	267.2	-27.2
G1.9+0.3	13407	48.4	2011-07-18	267.2	-27.2
G1.9+0.3	13509	55.3	2011-07-22	267.2	-27.2
G1.9+0.3	16947	38.8	2015-05-04	267.2	-27.2
G1.9+0.3	16948	39.6	2015-07-14	267.2	-27.2
G1.9+0.3	16949	9.1	2015-05-20	267.2	-27.2
G1.9+0.3	17651	111.6	2015-05-05	267.2	-27.2
G1.9+0.3	17652	26.2	2015-05-09	267.2	-27.2
G1.9+0.3	17663	56.5	2015-07-24	267.2	-27.2
G1.9+0.3	17699	19.8	2015-07-17	267.2	-27.2
G1.9+0.3	17700	14.9	2015-08-31	267.2	-27.2

Name	Obs ID	Effective Time (ks)	Date	R.A. (deg)	Decl. (deg)
G1.9+0.3	17702	36.9	2015-07-15	267.2	-27.2
G1.9+0.3	17705	9.9	2015-07-25	267.2	-27.2
Total		1805.5			
G330.2+1.0	6687	50.0	2006-05-21	240.2	-51.6
G330.2+1.0	19163	74.1	2017-05-02	240.2	-51.6
G330.2+1.0	20068	74.1	2017-05-05	240.2	-51.6
Total		198.2			
Kepler	116	48.8	2000-06-30	262.7	-21.5
Kepler	4650	46.2	2004-10-26	262.7	-21.5
Kepler	6714	157.8	2006-04-27	262.7	-21.4
Kepler	6715	159.1	2006-08-03	262.7	-21.5
Kepler	6716	158.0	2006-05-05	262.7	-21.4
Kepler	6717	106.8	2006-07-13	262.7	-21.5
Kepler	6718	107.8	2006-07-21	262.7	-21.5
Kepler	6719	87.8	2006-07-23	262.7	-21.5
Total		632.1			
Tycho	10438	50.7	2009-04-26	6.3	64.1
Tycho	10439	137.8	2009-04-16	6.3	64.1
Tycho	10440	137.0	2009-04-20	6.3	64.1
Tycho	10982	37.4	2010-03-20	6.3	64.1
Tycho	14643	31.1	2011-04-29	6.3	64.1
Tycho	16443	65.1	2012-04-13	6.3	64.1
Tycho	16832	81.8	2013-09-22	6.3	64.1
Total		931.0			
RX J1713.7-3946	7973	51.3	2007-03-20	258.3	-39.0
RX J1713.7-3946	16825	62.3	2013-04-29	258.3	-39.0
RX J1713.7-3946	16826	82.5	2013-04-25	258.3	-39.0
RX J1713.7-3946	16827	39.1	2013-04-24	258.3	-39.0
RX J1713.7-3946	16828	56.5	2013-04-27	258.3	-39.0
RX J1713.7-3946	16829	66.5	2013-04-28	258.3	-39.0
RX J1713.7-3946	16830	57.3	2013-04-26	258.3	-39.0
RX J1713.7-3946	16831	62.0	2013-04-30	258.3	-39.0
RX J1713.7-3946	16832	53.7	2013-04-23	258.3	-39.0
RX J1713.7-3946	16833	39.0	2013-04-31	258.3	-39.0
Total		428.8			
SN 1006	1248	22.4	2000-06-16	175.0	-41.8
SN 1006	4518	91.6	2004-10-09	175.0	-41.8
SN 1006	4519	45.3	2004-10-13	175.0	-41.8
SN 1006	4520	46.6	2004-10-10	175.0	-41.8
SN 1006	4521	38.6	2004-10-12	175.0	-41.8

Name	Obs ID	Effective Time (ks)	Date	R.A. (deg)	Decl. (deg)
SN 1006	4793	105.7	2005-09-02	175.0	-41.8
SN 1006	4794	25.0	2005-09-03	175.0	-41.8
SN 1006	4795	18.7	2005-09-03	175.0	-41.8
Total		438.4			
RCW 86	1993	92.0	2001-02-01	220.2	-62.7
RCW 86 NE	4611	71.7	2004-06-15	221.3	-62.4
RCW 86 NE	7642	69.2	2007-06-20	221.3	-62.3
RCW 86	10699	2.0	2009-06-14	220.5	-62.6
RCW 86	13748	36.1	2013-02-14	220.1	-62.7
RCW 86	14890	26.7	2013-02-03	220.4	-62.2
RCW 86	15608	29.2	2013-02-05	220.4	-62.2
RCW 86	15609	37.6	2013-02-10	220.4	-62.2
RCW 86	15610	23.1	2013-02-17	220.1	-62.7
RCW 86	15611	25.9	2013-02-12	220.1	-62.7
RCW 86 NE	16952	67.2	2015-06-25	221.3	-62.4
Total		560.3			
SN 1987A	14697	67.6	2013-03-21	83.9	-69.3
SN 1987A	14698	68.5	2013-09-28	83.9	-69.3
SN 1987A	15809	70.5	2014-03-19	83.9	-69.3
SN 1987A	15810	48.3	2014-09-20	83.9	-69.3
SN 1987A	17415	19.4	2014-09-17	83.9	-69.3
Total		274.3			
Vela Jr. NW	3846	39.5	2003-01-05	132.3	-45.6
Vela Jr. NW	4414	34.5	2003-01-06	132.3	-45.6
Vela Jr. NORTH	9123	39.7	2008-08-31	132.3	-45.7
Total		113.7			
HESS J1731-347	9139	29.2	2008-04-28	263.0	-34.7
Total		29.2			

Table A.2: Table Log for NuSTAR Observations

Name	Obs ID	Effective Time (ks)	Date	R.A.(deg)	Decl. (deg)
G1.9+0.3	40001015003	85.4	2007-02-10	267.2	-27.2
G1.9+0.3	40001015005	121.6	2007-03-03	267.2	-27.2
G1.9+0.3	40001015007	144.7	2009-07-23	267.2	-27.2
(Total)		351.7			
SN1006 NE	40110001002	35.4	2009-07-13	267.2	-27.2
SN1006 SW	40110002002	82.1	2009-07-26	267.2	-27.2
(Total)		155.6			0
RX J1713.73946 NW	40111001002	48.2	2011-05-16	267.2	-27.2
RX J1713.73946 NW	40111002002	184.0	2011-05-09	267.2	-27.2
(Total)		162.6			
Vela Jr. NW	40101011002	127.5	2011-05-18	267.2	-27.2
Vela Jr. NW	40101011004	159.3	2011-05-20	267.2	-27.2
(Total)		39.5			
SN1987A	40001014002	48.4	2011-07-18	267.2	-27.2
SN1987A	40001014003	55.3	2011-07-22	267.2	-27.2
SN1987A	40001014004	38.8	2015-05-04	267.2	-27.2
SN1987A	40001014006	39.6	2015-07-14	267.2	-27.2
SN1987A	40001014007	9.1	2015-05-20	267.2	-27.2
SN1987A	40001014010	111.6	2015-05-05	267.2	-27.2
SN1987A	40001014013	26.2	2015-05-09	267.2	-27.2
SN1987A	40001014015	56.5	2015-07-24	267.2	-27.2
SN1987A	40001014016	19.8	2015-07-17	267.2	-27.2
SN1987A	40001014018	14.9	2015-08-31	267.2	-27.2
SN1987A	40001014020	36.9	2015-07-15	267.2	-27.2
SN1987A	40001014023	9.9	2015-07-25	267.2	-27.2
(Total)		198.2			

Appendix B

Thermal Parameters

99

Tables B.1 and B.2 presents parameters of thermal model that was used for fitting the spectra of Kepler, Tycho, SN 1006, RCW 86, and SN 1987A in addition to the ZA07 and SRCUT models (see Tables 4.2 and 4.3 for the nonthermal parameters).

Table B.1: Thermal Parameters of ZA0 Model

Region	kT (keV)	O (O_{\odot})	Ne (Ne_{\odot})	Mg (Mg_{\odot})	Si (Si_{\odot})	S (S_{\odot})	Ar (Ar_{\odot})	Ca (Ca_{\odot})	Fe (Fe_{\odot})	Norm ($10^{-5} cm^{-5}$)
SN 1987A(Whole)	$10.6 \pm 0.5/0.68 \pm 0.03$	0.34	3.0	1.0	1.4	2.5	2.7	1.0	0.61	$37.64 \pm 3.113/35 \pm 2.50$
Kepler	0.53	1.0	1.0	1.0	44	28	130.8	1.0	1.0	0.15 ± 0.06
Tycho	0.38 ± 0.02	5.5	1.0	5.1	68 ± 13	54 ± 11	65	1.0	1.0	1.2 ± 0.3
SN 1006	3.23 ± 0.65	4.4	1.5	15.0	50	1.0	1.0	1.0	1.0	1.50 ± 0.50
RCW 86(NE)	0.44	1	1.9	1.9	1.9	1	1	1.2	1	17.0 ± 1.0

Note. The parameter values given without uncertainties are consistent and fixed in Tables B.1 and B.2. For the thermal model, VNEI is applicable to Kepler and Tycho, whereas Vpshock is utilized for SN1006 and RCW 86. In the case of SN 1987A, the initial and secondary terms of kT and Norm represent the

Table B.2: Thermal Parameters of SRCUT Model

Region	kT (keV)	O (O_{\odot})	Ne (Ne_{\odot})	Mg (Mg_{\odot})	Si (Si_{\odot})	S (S_{\odot})	Ar (Ar_{\odot})	Ca (Ca_{\odot})	Fe (Fe_{\odot})	Norm ($10^{-5} cm^{-5}$)
SN 1987A(Whole)	$1.48 \pm 0.02/2.5 \pm 0.2$	0.34	3.0	1.0	1.4	2.5	2.7	1.0	0.61	$50.0 \pm 3.11/35 \pm 2.5$
Kepler	0.53	1.0	1.0	1.0	44	28	130.8	1.0	1.0	8.37 ± 0.399
Tycho	2.52	5.5	1.0	5.1	68 ± 13	54 ± 11	65	1.0	1.0	3.5 ± 1.7
SN 1006	2.51 ± 0.45	4.4	1.5	15.0	50	1.0	1.0	1.0	1.0	8.67 ± 0.97
RCW 86(NE)	0.44	1	1.9	1.9	1.9	1	1	1.2	1	30.4 ± 2.02

optimal parameters for the Vequil and Vpshock models, respectively.